

DEVELOPMENT OF A TECHNIQUE TO LOCALIZE AND
QUANTIFY VOLUMETRIC LOW-LEVEL WASTE FROM
CANDU PLANTS

DEVELOPMENT OF A TECHNIQUE TO LOCALIZE AND QUANTIFY
VOLUMETRIC LOW-LEVEL WASTE FROM CANDU PLANTS

BY

PEIXIAO ZHOU, B.Sc.

A THESIS SUBMITTED TO THE DEPARTMENT OF RADIATION SCIENCE AND THE
SCHOOL OF GRADUATE STUDIES OF McMASTER UNIVERSITY

IN PARTIAL FULFILMENT OF THE REQUIREMENTS FOT THE DEGREE OF MASTER
OF SCIENCE

© Copyright by Peixiao Zhou, June 2023

All Rights Reserved

MASTER OF SCIENCE (2023)

McMaster University

(Radiation Science)

Hamilton, Ontario, Canada

TITLE: Development of a Technique to Localize and Quantify
 Volumetric Low-Level Waste from CANDU Plants

AUTHOR: Peixiao Zhou

 B.Sc. (Medical Physics)

 McMaster University, Hamilton, Canada

SUPERVISOR: Dr. Soo Hyun Byun

NUMBER OF PAGES: ix, 94

Abstract

With the complex composition of the radioisotopes and waste materials, the characterization of the volumetric low-level wastes from CANDU plants is challenging. This study presents a technique to localize and quantify the contaminations presented in the CANDU waste containers. MCNP-based models are developed for an N-type coaxial HPGe detector and a LaBr₃ detector to simulate the photon peak information. The simulated efficiency and the experimental count rates are combined to estimate the activity of unknown waste samples. During the spectrum collection of a 4L Marinelli beaker source and 1-quart waste samples, the MCNP algorithm showed better accuracy in activity estimation than the Mirion ISOCS/LabSOCS software. With further development, this method has the potential to outperform the popular commercial software in estimating activity for volume sources with complex geometry and uneven distribution. The multi-detector array models with hotspot designs are also studied in this work to provide real-time information about the location and activity of the contamination inside the 2.2 m³ industrial low-level waste containers. The on-site measurements show promising results as the position of the contamination was able to be located within a volume of 61×40×34 cm. Overall, this technique has good potential to be utilized in the nuclear industry for large-volume low-level waste analysis.

Acknowledgments

It was an unreal experience to go through a brand new Medical and Biological Physics undergraduate program, complete two 8-month co-op terms, navigate through the surreal Covid-19 pandemic, and participate the fascinating graduate study works for the past seven years at McMaster. Without the people around me, reaching this stage would not have been possible.

I want to express my deep appreciation and respect for my supervisor Dr. Soo Hyun Byun. Your knowledge, passion, and self-discipline have inspired me to keep moving forward. It was my honor to be your student and work alongside you. I would also like to extend my gratitude to Dr. Alan Chen and Dr. Jovica Atanackovic for being on my committee and providing comments on my work.

I am grateful to everyone in the McMaster Health Physics, McMaster Nuclear Operations & Facilities, and Laurentis Energy Partners that have contributed to the project. Especially for Mr. Ryan Cooke, Mr. Lionel Fernandes, and Ms. Ye Eun Kim to put up with all my requests and planning for the on-site activities. Of course, I want to thank my Byun group fellows as well. Your advice and supports keep me moving through this degree.

Last but certainly not least, I would like to shout out to my family and friends. Without your love, support, and accompany, I will not survive this long journey and I will not be who I am today.

Contents

Abstract	iii
Acknowledgments	iv
Chapter 1: Introduction	1
1.1 Low-Level Radioactive Wastes in Ontario	1
1.2 The LEP and the CMSR Project	2
1.3 Project Goals and Methods	4
1.4 Previous Studies on LLW Measurement	7
1.5 Gamma Spectrometers	9
1.6 Thesis Outline	12
Chapter 2: Gamma-Ray Spectrometer System and Experimental Samples	13
2.1 HPGe Detector Specification	13
2.2 Data Acquisition System	15
2.3 LaBr3 Detection System and Spectrum Analysis System	21
2.4 Measured Samples Information	23
Chapter 3: Monte Carlo Modeling Design	27
3.1 The Monte Carlo Simulation	27
3.2 Detector Geometry and algorithm validation	28
3.3 Deadlayer thickness estimation	32
3.4 Source geometry and distribution	33
3.5 Multi-detector array design	36
3.6 LaBr3 Detector	38
Chapter 4: Simulation Accuracy Validation	41
4.1 Detector efficiency test with point and disk sources	41
4.2 Detector efficiency test with volume sources	46
4.3 Model application on the 1-quart waste sample container	56
Chapter 5: Extensive Study on Volume Source Distribution	61
5.1 Detector efficiency dependence on volume geometry	61
5.2 Waste container materials simulation	63
5.3 Hotspot Simulation and Detector Array Design	68

5.4	Detector Array Response Analysis	71
5.5	Blind Test for Array 1 Model.....	77
5.6	LEP waste container measurement and comparison with hotspot model	79
Chapter 6: Conclusion and Future Works.....		88
6.1	Conclusion.....	88
6.2	Future Work.....	89
Bibliography.....		90
Appendix		93

List of Figures

<i>Figure 1: The summary of the CMSR project</i>	3
<i>Figure 2: The geometry of the P-type HPGe detector</i>	14
<i>Figure 3: The Ortec N-type HPGe detector used for in-lab measurement</i>	15
<i>Figure 4: The Ortec DSPEC Plus gamma spectrometry system</i>	16
<i>Figure 5: The energy calibration for the 1173 keV peak from a 10-min Co-60 spectrum</i>	17
<i>Figure 6: The peak fitting process by Maestro</i>	18
<i>Figure 7: The unsuccessful fitting and the manual fitting of the 664 keV peak</i>	19
<i>Figure 8: The successful Maestro fitting and the manual fitting of the 1112 keV peak</i>	20
<i>Figure 9: The BrillLanCe™ 380 LaBr3 detection system with and without preamplifier</i>	21
<i>Figure 10: The ROI analysis function using the CoMPASS software</i>	22
<i>Figure 11: The measurement of Na-24 volume source</i>	25
<i>Figure 12: The containers filled with contaminated masslin cloths</i>	26
<i>Figure 13: The geometry information for the waste containers on the LEP segregation site</i> ...	26
<i>Figure 14: The Ortec SN40P HPGe detector model built in MCNP6.2</i>	30
<i>Figure 15: The SN40-P HPGe detector energy efficiency curve simulated by EGS5 and MCNP6.2</i>	31
<i>Figure 16: The Ortec GMX 25-N coaxial HPGe detector on the x-z plane and the 3D structure of the detector</i>	32
<i>Figure 17: LLW bins' material composition</i>	36
<i>Figure 18: The MCNP 3D structure of the LaBr3 detector</i>	39
<i>Figure 19: The energy efficiency curve for point sources at 25 cm</i>	42
<i>Figure 20: Point source measurement at 25 cm using Eu-152 and Cs-137 with curve fitting</i> ...	44
<i>Figure 21: Disk source measured efficiency and simulated efficiency at 25 cm</i>	46
<i>Figure 22: The 3D structure of the setup in MCNP</i>	48
<i>Figure 23: Experimental efficiency and simulated efficiency for the 4 L Marinelli beaker</i>	49
<i>Figure 24: The expected activity of Eu-154, Eu-155, and Sb-125 in the Marinelli beaker compared with the activity predicted using MCNP algorithm and LabSOCS software</i>	51
<i>Figure 25: The MCNP geometry for the detector and the 500 mL Na-24 volume sample</i>	53
<i>Figure 26: The MCNP model for upright and reversed geometries</i>	58
<i>Figure 27: The predicted activity of Cs-137 within each volume sample using three different models</i>	60
<i>Figure 28: The 3D view of the 7d1s model and the 5d5s model</i>	62
<i>Figure 29: The combined absolute efficiency of different detector distributions</i>	63
<i>Figure 30: The detector efficiency on 662, 1173, and 1332 keV peaks for different densities of 7 waste compositions relative to the Group 1 efficiency</i>	66
<i>Figure 31: Absolute efficiency comparison between Group 1 and Group 7 materials at various filling densities</i>	68
<i>Figure 32: The 2D plot for hotspot location of #1 and #18 in Visual Editor software</i>	70
<i>Figure 33: The 3D structure of multi-detector Array 1 and Array 2</i>	71

<i>Figure 34: Detector efficiency as a function of hotspot center location for the 0.2 g/cm³ model</i>	72
<i>Figure 35: Detector efficiency as a function of hotspot center location for the 0.5 g/cm³ model</i>	74
<i>Figure 36: The 2D plot for the updated hotspot location of #1 and #18 in Visual Editor software</i>	80
<i>Figure 37: The location of the hotspot for on-site measurement</i>	83
<i>Figure 38: Gamma spectrum acquirement process at the top center position</i>	84
<i>Figure 39: The 5-minute gamma spectrometry collected at the center of the back surface</i>	84

List of Tables

<i>Table 1: The parameter setup for the system</i>	16
<i>Table 2: The comparison between the peak fitting parameters output from Maestro and MATLAB</i>	20
<i>Table 3: Parameters setup for the LaBr3 system</i>	22
<i>Table 4: The information for the standard calibration sources used in the experiments</i>	23
<i>Table 5: The geometries for the sources</i>	33
<i>Table 6: MCNP material card design for measured sources</i>	36
<i>Table 7: The detector array design on waste container measurement</i>	37
<i>Table 8: Comparison of the Simulated Absolute Peak Efficiency of a Co-60 Point Source at 20cm</i>	40
<i>Table 9: Na-24 Volume Sample Activity Prediction with Various System</i>	53
<i>Table 10: CMSR waste streams and the sample materials</i>	64
<i>Table 11: Seven groups of waste combination with the material information</i>	64
<i>Table 12: The absolute efficiency of each detector position on hotspots relative to the front detector</i>	75
<i>Table 13: The absolute efficiency relative to the center detector (#2) at each surface</i>	77
<i>Table 14: The Hotspot Locations used for the blind test and the simulation result</i>	77
<i>Table 15: Information for the measured container</i>	79
<i>Table 16: The absolute efficiency of each detector position on the new hotspots model for 662 keV and 1173 keV photons</i>	81
<i>Table 17: The ratio of the count rate at each location relative to the top location</i>	84

Chapter 1: Introduction

1.1 Low-Level Radioactive Wastes in Ontario

In Ontario, approximately 60% of the electricity is generated from nuclear power plants [1]. During the reactor maintenance, many low-level radioactive wastes (LLW) are produced, including contaminated tools and likely contaminated personal items [2]. The LLWs are classified into long-lived and short-lived based on their radioactive half-lives, and they will need to be disposed through different pathways. The shorter-lived ones can be stored in temporary sites, when their activities are decayed below a certain limit, they will be surveyed and disposed through various pathways. For long-lived wastes, they are likely to be stored in an authorized facility, such as near-surface waste management site [3].

Despite being classified as LLW, a large portion of the nuclear by-product are found to be radiation-free. In Ontario, the cost of LLW storage can go as high as \$6,000 per year for a 1 m³ container. Therefore, the most economical and environmental-friendly way to process LLW is to ensure that all the non-contaminated waste is sorted out. Currently, these wastes must be sorted by hand for characterization all around the world. This method is certainly not ideal due to the time-consuming and labor-intensive process. The Clean Energy Materials Sorting & Recycling (CMSR) initiative by Laurentis Energy Partners (LEP) is aiming to discover new methods and technologies to characterize low-level wastes.

1.2 The LEP and the CMSR Project

Located in Hamilton, Ontario, the LEP's waste sorting site is actively surveying and characterizing a large quantity of low-level waste originating from Ontario Power Generation (OPG), where they have been stored for up to 30 years. They are alpha-beta-gamma mixed emitters produced through pipeline maintenance and daily operation, containing materials such as cleaning tools and Personal Protection Equipment (PPE). [4] During the sorting process, the waste bags are taken out from the original shipping containers to be surveyed and characterized by radiation surveyors. They are then segregated into different streams, including incinerable waste, compactable waste, non-processible waste, metal, and potentially free-releasable waste. The first four materials will be sent to designated facilities for disposal, while the potential free-releasable waste undergoes further surveying and characterization at a low-background area to ensure the radiation hazards are minimized.

The CMSR project is split into two phases: Phase 1 focuses on understanding the source term, meaning the type and activity of radioisotopes presented. Since all these wastes are generated at the same sites, the type and activity ratio of the radioisotopes should remain relatively consistent. By studying this thoroughly, a database can be built to predict the type and activity of radioisotopes in the waste container based on the decay storage time. Because some radiation particles, such as alpha particles, are much harder to detect compared to high-energy gamma rays, the

database will be a convenient way to predict the presence of alpha particles without manually surveying.

Phase 2 of the CMSR project aims to develop a real-time analysis method to determine the source term information in the waste container. The idea is to use the Monte Carlo (MC) simulation and the source term information collected to develop a new detection system. The system will contain a detector array consisting of different types of radiation detectors and a corresponding database to link the detection spectrum with the radioisotopes presented in the sample. This is where this MSc research project comes in. [Figure 1](#) shows a summary of the CMSR project.

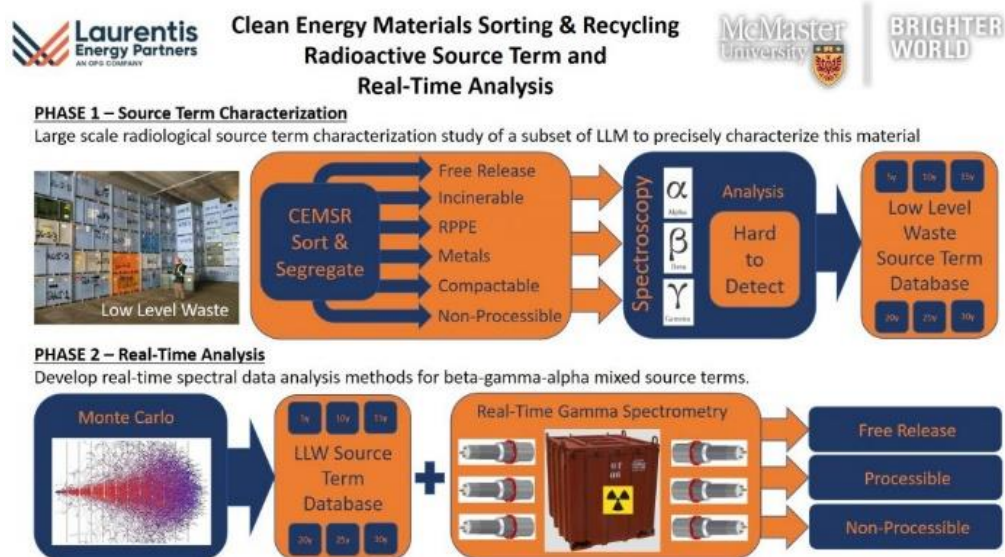


Figure 1: The summary of the CMSR project. [4]

1.3 Project Goals and Methods

This MSc project has two major goals. The first one is to develop a feasible MC model using the MCNP code to simulate detector responses for various source geometries. The second one is to develop a calibration method to correlate detector responses with contamination quantity and location in the volume waste.

To achieve the first goal, a benchmarking test is performed by comparing the MCNP simulated energy efficiency curve result to published data to verify the building algorithm. The verified algorithm is then applied to the HPGe detector model used in the experiment. The new model is further tested by simulating detector responses to six different standard calibration sources. Details of the MCNP simulation and experimental setup are provided in the next section.

To achieve the second goal, various volumetric source models are built and tested on MCNP to study detector responses to different source sizes and distributions. With the help of the segregation team, I added surveyed waste information to the model and tested the detector response under different conditions. I also built two detector arrays on MCNP to simulate hotspot scenarios in the container. One array had a single detector placed on different surfaces of the container, while the other was made up of three diagonally placed HPGe detectors. By comparing the simulated responses, a database is built to link the detector peak ratio to the location of the source. If this simulated ratio result is verified through actual experimental testing on waste containers, the detector array can be applied to the waste containers and

locate the contamination without opening them. With the density information of the container, the activity of the located contamination can then be estimated.

When comparing the detector responses on different source models, the source emission energy of 662 keV is used in most simulations. This energy corresponds to the Cs-137's gamma energy peak. It is chosen due to its high appearance frequency in the OPG waste stream. Since most of the wastes are generated through reactor operation, OPG samples the loose contamination from the pipelines regularly. The initial activity ratios (at year 0) of the presence of radioisotopes are recorded, and their ratios throughout each year of storage are then calculated based on the half-lives. Cs-137 is one of the most common radioisotopes from the nuclear waste cycle, and it is found in almost all LEP waste containers. With a half-life of approximately 30 years and an emission of 662 keV photons, Cs-137 can be easily detected in historical wastes. Therefore, if our method can accurately estimate the activity of Cs-137 presented in unknown OPG-generated wastes, the activities of other potentially presented radioisotopes can be calculated through the derived activity ratio. This will be very convenient since the alpha and beta emitters, which cannot be detected outside of the container, can now be estimated through the relative ratio to Cs-137.

In the current market of radiation detection technologies, the CANBERRA ISOCS (in Situ Object Counting System)/LabSOCS (Laboratory Sourceless Calibration Software) is one of the popular software for large volume sample activity measurement.

Similar to this project, it uses MCNP code and mathematical models for source

analysis. Combining a calibrated detector and the built-in source geometry models, the software can characterize and quantify the potential radioisotopes that exist in the source. I am fortunate to have access to the LabSOCS from the McMaster University Health Physics Department to test several homogeneous volume sources, and the software provided credible results. However, its accuracy can be greatly affected if the activity in the sample is distributed non-homogeneously. Even with the newly included Uncertainty Estimator tool (IUE), ISOCS required input of well-defined source data, such as source distribution information, to estimate the source information. Otherwise, the software will give a reliable range of activity, but the uncertainty will be too large for some extreme distribution cases, such as hotspots.

[6][7]

In this research, our approach with the detector array has the potential to outperform LabSOCS in LLW measurement. As mentioned previously, a large portion of the nuclear by-products analyzed at LEP is free of contamination. It indicates that most of the containers will not contain a full bin of evenly distributed radioactive waste. Therefore, it is more likely to see radioactive waste distributed in the form of hotspots inside the containers. By comparing the gamma spectrums collected on different sides of the waste container, the hotspots can be located. Then the activity can be estimated using the waste density and the detector energy efficiency.

1.4 Previous Studies on LLW Measurement

Many techniques are used in the nuclear industry to analyze radioactive waste information. Destructive measurement is the most accurate method to characterize and quantify the radioisotope components in the wastes. A representative sample needs to be selected from the waste, which is then chemically and radiochemically treated to provide radionuclide data. However, this method will not be ideal for heterogeneous wastes. The high complexity of the waste stream information is the main challenge for representative sample collection. [8]

The non-destructive methods are performed by examining the physical properties of the waste samples. Without the need to obtain a representative sample, this method is preferred for heterogeneous and bulky wastes. The examination can be performed in active and passive ways. The active measurements utilize external radiation sources such as photons and neutrons to analyze source information. The high-photon radiography/tomography is a technique that provides rich details of the waste. This method requires a LINAC to generate high-energy photons that scan the waste sample similar to a medical radiography. A 2D or 3D graph can be reconstructed which shows the geometry and density of internal components in the waste sample. In practice, it has been proven to handle waste samples up to 5 tons. [9] However, the utilization of LINAC introduces additional radiation safety concerns in the facility, which introduces some concerns.

Passive measurement is the most often used method in the radiation safety field due to its simplicity. The measurements are performed by passively detecting the radiation spectrum emitted to predict the source term. [10] Depending on the emitter, the spectrum of photons or charged particles can be collected. For homogeneous waste samples, calibration software such as ISOCS is commonly used for stationary measurement. As mentioned in Section 1.3, this type of software can be calibrated to different detectors. Using the built-in source geometry algorithm, it can interpret the collected spectrum to predict the activity of the objects. For waste samples with non-uniform density and radioisotope distribution, the segmented gamma scanning (SGS) technique is widely used. With a collimator attached, the detector collects the spectrum information in different sections of the volume along the vertical and horizontal directions. Using deconvolution and MC simulation, a 2D activity distribution of the sample can be constructed. With a more advanced computation algorithm, photon emission tomography can be combined with segmented gamma scanning, which constructs a 3D view of the activity distribution inside the measured volume. This technique can be used in imaging spent-fuel bundles, as well as volumetric wastes. [11] A 2015 study demonstrated the accuracy of the SGS methods on a 210 L drum, where the gamma sources are corrected and located in a 20×20 pixels tomography, and the activity is predicted with less than 10% discrepancy. [12]

The approach for this research project is similar to the SGS method. The gamma spectrum collection at different locations can provide distribution information of the

radioisotopes, while the simpler spectrum processing procedure can reduce calculation complexity.

1.5 Gamma Spectrometers

To collect the source information from the waste, the radiation detector is an essential component in this research. There are many types of radiation detectors available in the industry for gamma-ray detection, including ionization chambers, proportional counters, Geiger-Muller tubes, scintillation detectors, and semiconductor detectors. The fundamental principles for them are similar; they transfer the incoming photon energy into secondary particles and finally are converted into electric signals for detection. The most often used detector in this MSc project is a High-Purity Germanium (HPGe) detector and a Lanthanum Bromide $\text{LaBr}_3(\text{Ce})$ detector. [13]

The HPGe detector is a type of semiconductor detector. The semiconductor materials are Group IV atoms in the periodic table, which have 4 valence electrons in the outer shell. In this material, the bandgap between the valence band and the conduction band is smaller than the insulator so that the electron can cross the bandgap to make it conductive under certain circumstances. Based on the doping material, the semiconductor can be classified into p-type and n-type. The P-type semiconductor is doped with Group III, which has holes as charge carriers; while the n-type semiconductor is doped with Group V atoms and has excess electrons as charge

carriers. When the p-type and n-type semiconductors are put together, a p-n junction diode is created. With an applied voltage, the charge carriers (electrons and holes) from two ends will diffuse to the other side and recombine to create the depletion region that acts as the radiation detector. When an incoming energetic particle (radiation) interacts and deposits its kinetic energy to the depletion region, the material is ionized, and the electron-hole pairs are created. The pulses will be created in the circuit as electron-hole pairs being produced for the detection system to pick up. Comparing to a gas-filled detector, which is another type of detector that uses gas as the medium to create electron-ion pairs, the semiconductor detector has a better energy resolution. The average energy required to ionize the air, also known as the w-value, is approximately 34 eV, while the w-value for a germanium detector is approximately 3 eV. As a result, the semiconductor will generate more electrons for detection when radiation enters the material.

On the other hand, the LaBr_3 detector is a type of inorganic scintillation detector. The detector consists of the scintillator and the photomultiplier tube (PMT). As the radiation particles interact with and deposit their kinetic energy to the scintillator, the electrons will travel from the valence band to the conduction band. The de-excitation process then happens with the electrons returning to the valence band and emitting energy as visible light. The activators are added into the scintillator crystal to increase the photon emission efficiency, as they introduce more energy states in the crystal to emit multiple photons during the de-excitation process. For example, Cerium (Ce) is usually added to the LaBr_3 crystal as the activator. The

photons then enter the PMT and interact with the photocathode. The photocathode can transfer the incident photons into electrons through the photoelectric effect. The focused photoelectrons are then multiplied in the PMT to create a current for signal detection.

As mentioned above, the HPGe detector is the designated detector used in this research project for both experimental measurement and simulation. It was chosen because of its superior efficiency and resolution. The Ge detector can provide more peak information with smaller full width at half maximum (FWHM) values. This makes HPGe the best contender for this research project, as I want to use energy information to determine the possible photon emitter. However, the HPGe detectors have limitations. First, the production of the HPGe detector is challenging, as the crystals need to be grown under a controlled environment. The limited number of manufacturers in the world also keeps the price high. Furthermore, the HPGe detectors require a cooling system. To maintain the semiconductor properties, the Germanium crystal needs to be kept at 77 Kelvin. The more common way is to attach the detector to a liquid nitrogen tank, which makes the detection system not portable and almost impossible to bring to the LEP waste storage site for real-time measurement. There are options for portable HPGe detectors available on the market, but the electrical cooling system keeps the price high. For this project, a detector that is portable and has good energy resolution will be ideal. The BRILLIANCE B380 is a 2'x2' LaBr₃ detector that is available at McMaster University. The simplified detection system consists of a detector, an HV unit, a digitizer, and a

data collection laptop. This unit is the best option for us to bring into the LEP waste storage site for real-time measurement.

1.6 Thesis Outline

Chapter 1 introduces the motivation and goal of this project, including the background information on low-level waste production and the CMSR project.

Chapter 2 introduces the data collection system and other materials used in experiments. Chapter 3 covers the Monte Carlo simulation models built on the MCNP platform. Chapter 4 describes the validation process of the MCNP model by comparing the simulated result with the experimental result and LabSOCS measurement result. Chapter 5 discusses the extensive study on localizing contamination in industrial waste containers using different detector arrays.

Chapter 6 summarizes and concludes the study.

Chapter 2: Gamma-Ray Spectrometer System and Experimental Samples

2.1 HPGe Detector Specification

The detector used in this research is the Ortec Gamma-X (GMX) N-type HPGe coaxial detector. The N-type structure has the inactive crystal volume, also known as the deadlayer, at the inner surface of the crystal. Lithium is usually dosed at the inner surface as the n^+ contact through lithium drifting technique, and Boron is dosed at the outer surface as the p^+ contact through ion implantation. Such techniques will result in the doped Boron layer being much thinner than the doped Lithium layer, which allows it to detect photon energy as low as 3 keV. As a comparison, the P-type coaxial detector with a deadlayer located at the outside surface can detect photon energy as low as 40 keV [14]. The wide detection range makes this detector a great choice for gamma spectrometry for unknown wastes.

Based on the detector drawing provided by Ortec (shown in [Figure 2](#)), the coaxial-shaped Germanium crystal is doped with 700 microns of lithium at the hole contact side and 0.3 microns of boron at the outside. The crystal is mounted on aluminum and shielded by an end cap made with aluminum and beryllium. Despite the active detection volume being less than a 5 cm diameter by 10 cm long cylinder, the attached dewar for liquid nitrogen storage limits the mobility greatly. The front end of the detector is pointed to an attached stand for source placement. A plastic rack with specially designed plastic dividers can be used to hold smaller sources in

various shapes. The picture of the detection equipment is shown in [Figure 3](#).

Referring to the QA datasheet provided, the detector has an FWHM of 1.78 keV at 1.33 MeV and a relative efficiency of 14.4%. This information will be used to assist the MCNP model building.

GERMANIUM DETECTOR DIAGRAM

SERIAL NUMBER 25-N1505B

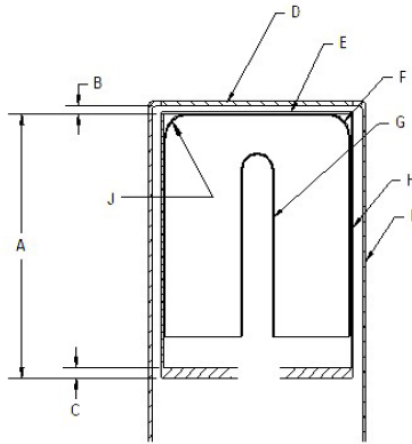


Figure 2: The geometry of the detector. H - Al mount cap wall, I - Al end cap wall, F - boron layer, G - lithium layer, E - mylar as an insulator, D - beryllium end cap window.



Figure 3: The Ortec N-type HPGe detector used for in-lab measurement. The detector part is attached to the blue LN2 dewar, shown on the left. The source holding rack is shown on the right.

2.2 Data Acquisition System

The detector is connected to the Ortec DSPEC Plus MCA workstation for signal process ([Figure 4](#)). Before collecting the data, the appropriate input parameter values need to be chosen to maximize the resolution. The input pulse is modeled into a quasi-trapezoid shape controlled by rise time, cusp, flattop, and tilt. These values describe the rise and fall of the input pulse, the curvature of the quasi-trapezoid shape, the width of the shape, and the slope of the flattop, accordingly. A larger value of rise time and flattop can increase the resolution of the system but might decrease the efficiency if the count rate is high. In most of our measurements, the source is measured at 25 cm from the detector surface, which results in low deadtime (<0.2%). Therefore, the detector efficiency will not be affected by the higher setting value. Tilt value is usually optimized by DSPEC for the best resolution. [15] The Amplifier Gain can shift the energy peaks on the spectrum, which changes the energy

range displayed by each channel. A higher amplifier gain can express more energy information but requires a longer counting time to reach the same peak area for analysis. In our measurements, the amplifier gain is set to 1.00 to display max energy at approximately 2700 keV. The analog-to-digital converter (ADC) converts the signal into energy channels. The total channel number for a gamma spectrum can be controlled by the ADC gain. In our experiments, the ADC gain is set to 16384 to display 16k channels. All the setup parameters are summarized in [Table 1](#).

Table 1: The parameter setup for the system

Parameter	Setting Value
Rise Time	2.00 μ s
Cusp	1.00 μ s
Flattop	2.40 μ s
Tilt	-0.10938
Amplifier Gain	1.00
ADC Gain	16384



Figure 4: The Ortec DSPEC Plus gamma spectrometry system.

Maestro, the emulator software, is used to visualize and analyze the gamma spectrum. An energy calibration needs to be performed before the measurements to ensure the energy values are matched to the channel number. Am-241, Cs-137, Co-60, and Eu-152 standard calibration sources are usually used to calibrate the system due to their availability in the lab. [Figure 5](#) shows the energy calibration process using a Co-60 source. After significant peaks are shown in the spectrum (usually takes 10 minutes counting), the channel with the highest count will be set as the expected energy. With multiple photon peaks, a linear calibration curve will be established by the system to convert channel numbers into energy.

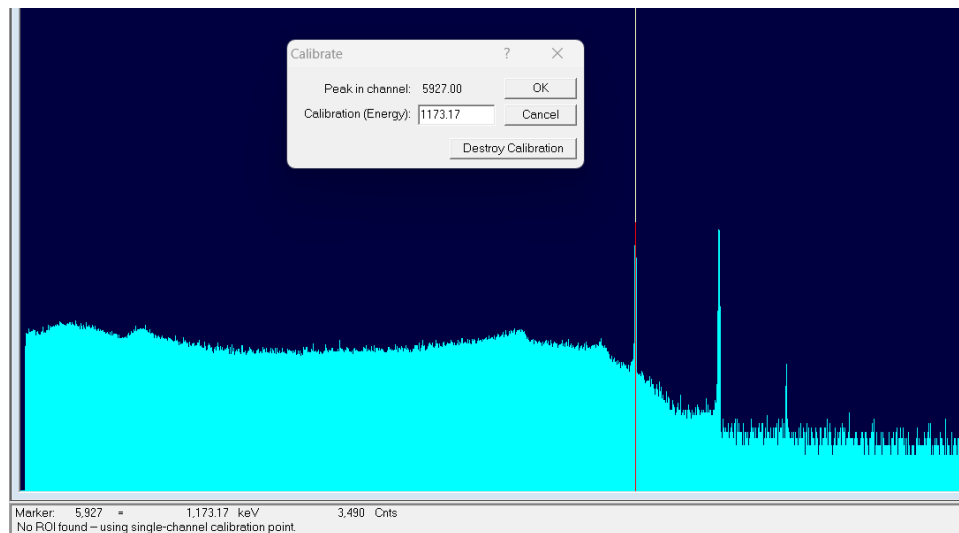


Figure 5: The energy calibration for the 1173 keV peak from a 10-min Co-60 spectrum.

After gamma spectrum collection, the Region of Interest (ROIs) can be selected manually or automatically through "Peak Search" at the peaks we are interested in. The "Peak Search" function highlights the channels within 3 times the FWHM value

as the peak region. After selecting the ROIs, the software will analyze them and provide peak details, including Peak Range, Centroid, Gross Area, and Net Area with uncertainty. The Gross Area is calculated by summing all the channels in the ROI. The Net Area is calculated by subtracting the Gross Area from the background level. A linear background level is calculated by connecting the midpoint fractional channel of the first and last n channels in an ROI, where n is the number of background points selected by the algorithm. The program then attempts a least-square fit of the Gaussian function to locate the centroid information. The calculation can be visualized in [Figure 6](#).

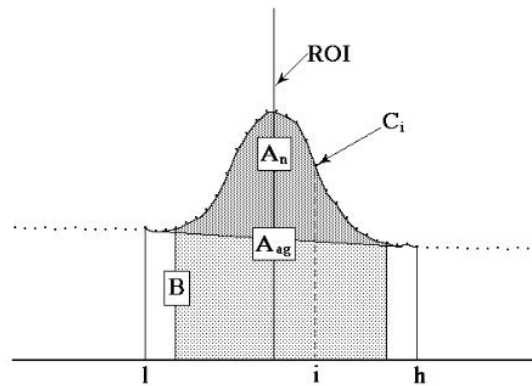


Figure 6: The peak fitting process by Maestro, where A_n is the net area, A_{ag} is the adjusted gross area, B is the background spectrum.

The Net Area of the peak is usually used to calculate detector efficiency in the experimental measurements. However, the “Peak Search” function does not always perform well. For example, in the presence of multiple overlapping peaks or high background counts, the Maestro algorithm does not output accurate peak areas. In

this case, manual fitting of the peak will be performed either through Maestro or Matlab. [Figure 7](#) is an example of failed automatic fitting as a comparison to the Matlab manual fitting of the 964 keV peak from Eu-152, where the FWHM and the area of the peak are greatly underestimated. Hence, the manual fitting result is the better choice for analysis.

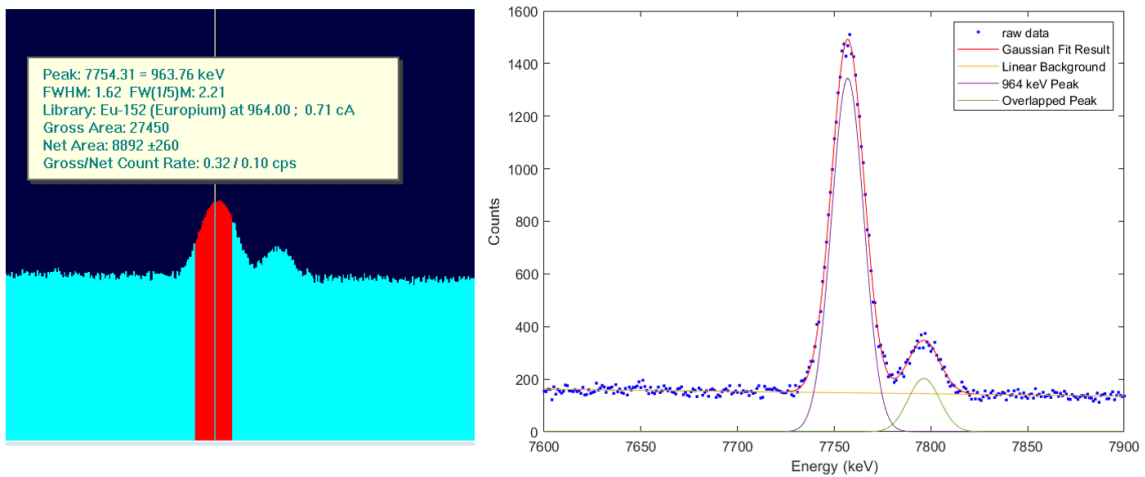


Figure 7: The unsuccessful (left) fitting and the manual fitting (right) of the 664 keV peak from a 24-hour measurement of the Eu-152 source. The manual fit is performed by fitting data to a double Gaussian function with a linear function to match the overlapped peaks and linear background.

A good fitting scenario is given in [Figure 8](#). When the peaks are well separated and the background is relatively consistent, the Maestro fitting algorithm can perform as well as a manual Gaussian fitting. The result of Maestro fitted parameters and the Matlab fitted parameters are listed in [Table 2](#). Matlab has a slightly higher peak resolution, as the FWHM is 3% lower than the Maestro result. However, Maestro peak analysis has a more accurate net area value with a much smaller uncertainty.

Overall, the fitted peak parameters output from Maestro and Matlab are comparable. For the consistency of data analysis, manual peak fitting using Matlab is adopted for the experimental gamma spectrum analysis.

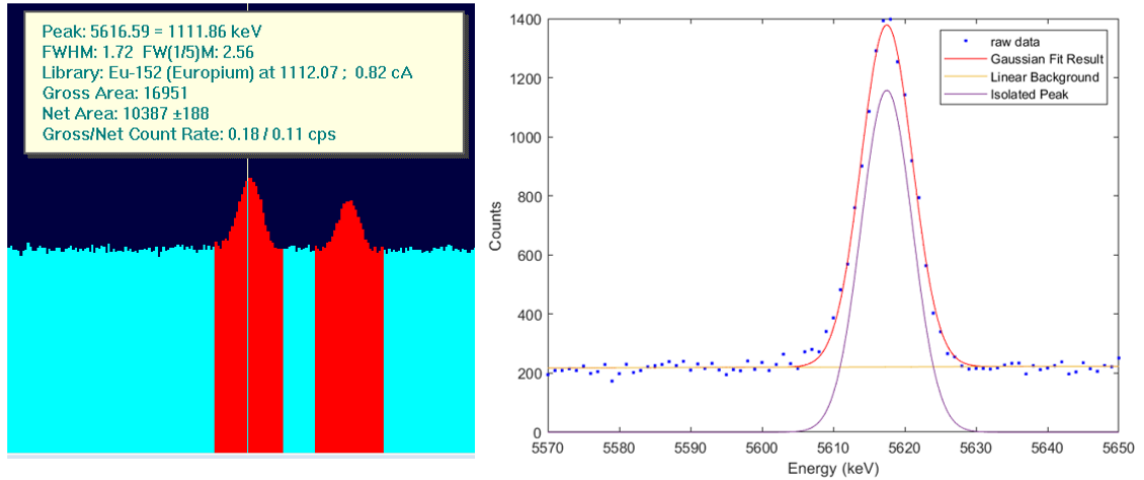


Figure 8: The successful (left) Maestro fitting and the manual fitting (right) of the 1112 keV peak from a 26-hour measurement of the Eu-152 disk source.

Table 2: The comparison between the peak fitting parameters output from Maestro and MATLAB

	Maestro (channel)	MATLAB (channel)
Range	5602-5630	5603-5630
Centroid	5616.59	5617
Gross Area	16951	16596
Net Area	10387 ± 188	10405 ± 532
FWHM	8.71	8.45

2.3 LaBr₃ Detection System and Spectrum Analysis System

The device we used for the on-site measurement with the low-level waste containers is the BrillanCe™ 380 2" x 2" LaBr₃(Ce) detector. The detector is paired with the HAMAMATSU C9525 high-voltage (HV) power supply and the CAEN DT5724 digitizer to form the detection system. The analysis software used is the CAEN CoMPASS, which has the ability to perform Gaussian fitting with linear background on the ROI. With the previous work by T. Ren[16], this system can function well without a preamplifier (preamp) or preamp power supply, which greatly enhances its portability. The system setup with the preamplifier is also tested referring to previous work by A. Laranjeiro [17], where the plugin preamp and the DT5423 preamp power supply are added to the system. The setup of the two systems is shown in [Figure 9](#), and the parameter setup is listed in [Table 3](#).

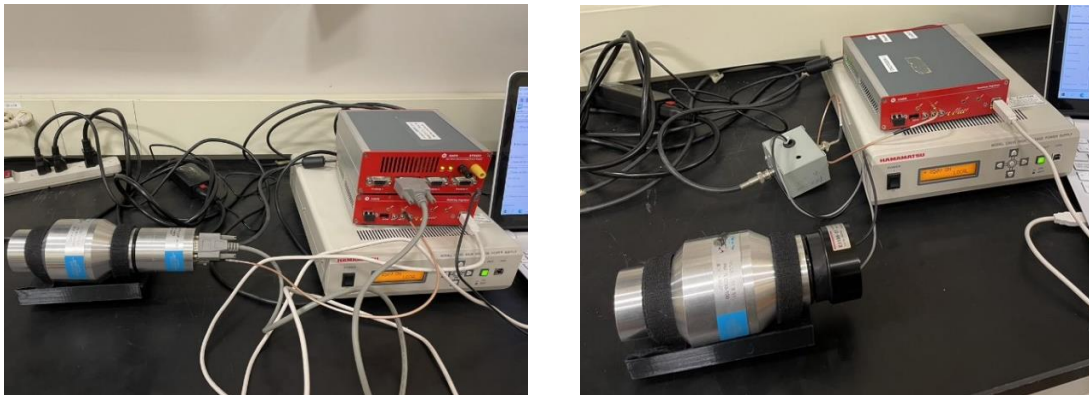


Figure 9: The BrillanCe™ 380 LaBr₃ detection system with (left) and without a (right) preamplifier.

Table 3: Parameters setup for the LaBr3 system

	Voltage	Channel Number	Rise/fall Time (us)	Flattop (us)	Threshold (lsb)	Resolution at 662 keV
With Preamp	850	2048	0.3	0.5	20	2.71%
Without Preamp	850	1024	0.1	0.1	50	3.71%

With the following system setting, the gamma spectrum collected can be analyzed on the CAEN CoPASS data acquisition software. As shown in [Figure 10](#), Gaussian fit will be performed on the manually selected ROIs with a linear background fit using the minimum chi square method. The peak information such as Net Count and FWHM will be calculated and used for source analysis.

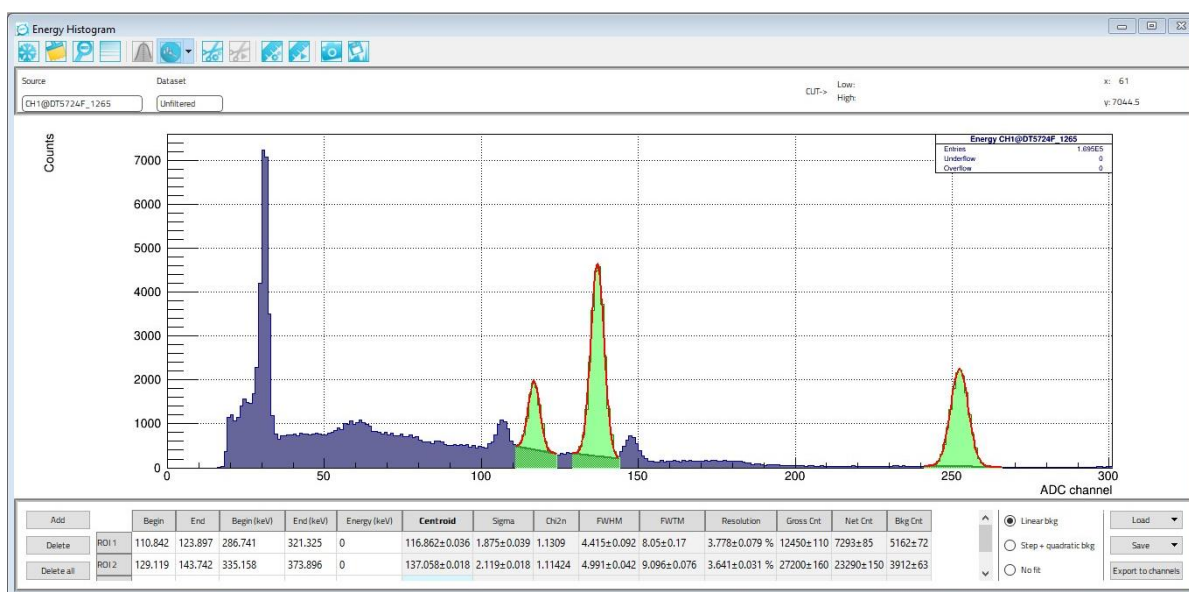


Figure 10: The ROI analysis function using the CoPASS software, where the Gaussian fit is applied with a linear background.

2.4 Measured Samples Information

In this project, the samples measured by the HPGe detector can be categorized into several groups: standard calibration sources, neutron-activated volume sources, and unknown waste sources.

The standard calibration sources used for model validation are borrowed from the McMaster Health Physics Department (HPD) and the McMaster Centre for Neutron Activation Analysis (NAA). We used these sources to validate the accuracy of the detector efficiency compared to the manufacturing document, as well as to compare the accuracy of our MCNP model on different source geometry. These sources include “point” source, disk source, and volume source with various geometries. The “point” sources are volume sources with very small dimensions. At a measurement distance of 25 cm from the detector surface, the solid angle effect on the volume can be negligible and hence can be considered as a true point source in the simulation. The information of the sources is listed in [Table 2](#).

Table 4: The information for the standard calibration sources used in the experiments.

Source Number	Manufacture	Source Type	Geometry	Calibration Date	Isotopes	Initial Activity
1	Eckert & Ziegler	“point”	4.75 mm diameter x 4.75 mm height	2011-04-01	Cs-137	500 nCi
2	Eckert & Ziegler	“point”	4.75 mm diameter x 4.75 mm height	2011-05-01	Eu-152	500 nCi
3	Canberra	Disk	50.8 mm diameter	2010-06-10	Co-60	32.012 kBq

4	Canberra	Disk	50.8 mm diameter	2010-06-10	Eu-152	8.510 kBq
					Eu-154	10.428 kBq
					Eu-155	14.038 kBq
5	Eckert & Ziegler 433N	4L Marinelli Beaker	3.25inchx8.3 cm (hole depth and diameter)	2016-02-01	Eu-154	15.01 kBq
					Eu-155	30.24 kBq
					Sb-125	29.43 kBq

Since the model is designed to measure volumetric wastes, we need to validate the MCNP model using sources with a larger volume. The Marinelli beaker is the only volumetric standard calibration source available in the department, but the complexity of the “endcap” structure can introduce more uncertainty into modeling. Therefore, we also made a volumetric cylinder source for measurement through neutron activation. This source is prepared by dissolving 0.0456 g of NaNO_3 powder into 1 mL of distilled water. Using the air-driven pneumatic system (the “rabbit” system) in the McMaster Nuclear Reactor, we performed a 10 s neutron irradiation of the sample to produce a Na-24 isotope. The activity of the 1 mL sample can be estimated using the detector point source efficiency. Following the radiation safety requirement from the HPD, the transfer of unsealed sources can be performed with activity below 1000 Bq. Therefore, the decayed source is transferred into a bottle filled with approximately 499 mL of water to create a 500 mL volume sample. The resulting volume source has a diameter of 7.2 cm and a height of 14 cm ([Figure 11](#)). To validate the radionuclides are evenly distributed into the volume, the spectrums of six consecutive 10-minute measurements are compared for indifference. Finally,

this source is ready to use for efficiency measurement, as well as the LabSOCS software calculation. Details of the experimental results can be found in **Chapter 4**.



Figure 11: The measurement of Na-24 volume source. In this figure, the bottle is placed 15 cm from the detector, and the center of the detector is lined up with the midline of the liquid.

After the validation of the detector efficiency on calibrated volume sources, the measurement of actual waste volume samples can proceed. Nine contaminated waste samples were sent from the LEP site for source characterization. The loose contamination found in the LLWs is collected using Masslin cloths and sealed in 1-quart plastic containers (**Figure 12**). Since the information on radioisotopes, source distribution, and activity are unknown, the estimated source terms are compared with LabSOCS simulated result. The results can be found in **Chapter 4**.

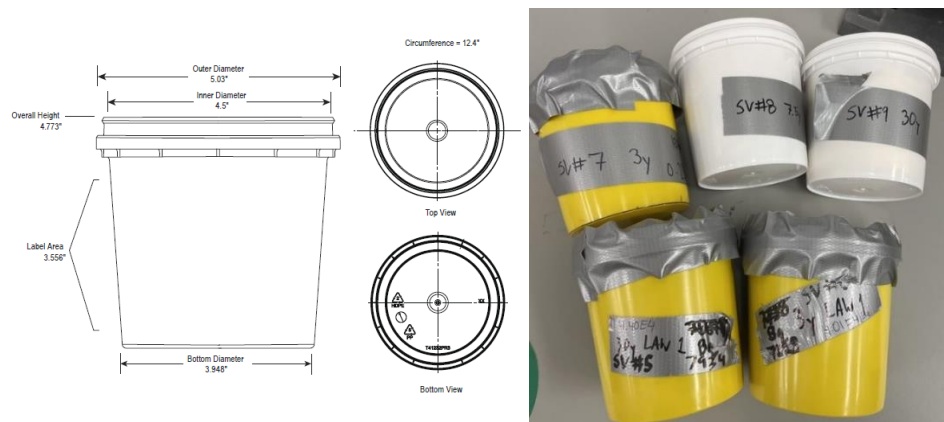


Figure 12: The containers filled with contaminated masslin cloths. Only Sample #5-9 are shown.

Finally, on-site measurement is performed for the industrial-size waste storage containers. The geometry information of the four types of containers on-site is listed in Figure 13. [18]

LLW Container	Dimensions (cm)	Volume (cm ³)	Shield Thickness (cm)*
Non-Processible Container (Blue)	Length (x): 182.88 Width (z): 119.38 Height (y): 102.39	2.24E+6	0.28
High Capacity Non-Processible Container (Green)	Length (x): 182.88 Width (z): 119.38 Height (y): 74.45	1.63E+6	0.28
B-1000 Box Compactor Container (Yellow)	Length (x): 176.21 Width (z): 116.84 Height (y): 119.38	2.46E+6	0.64**
Low Level Drum Container (Orange)	Length (x): 182.88 Width (z): 119.38 Height (y): 89.22	1.95E+6	0.28

Notes:

*Shield thickness in cm was based upon its gauge number and corresponding approximate thickness of steel sheet-metal [3].

**Value is based on the nominal thickness listed on the waste container.

Figure 13: The geometry information for the waste containers on the LEP segregation site.

Chapter 3: Monte Carlo Modeling Design

3.1 The Monte Carlo Simulation

The Monte Carlo (MC) Method is a computational algorithm developed by Nicholas Metropolis, John Von Neumann, and Stanislaw Ulam in the 1940s. Naming after the famous casino city in Monaco, it utilizes random processes to simulate the outcome of physical and mathematical models. In the case of radiation particles, the process of scattering and energy deposition can be simulated based on the probability of interaction.[19] In the application of a radiation detector, the MC method can be used to simulate the emitted radiation interaction with the detector's crystal to generate the gamma spectrum.

In this research, the Monte Carlo N-Particle (MCNP6.2) code is used to simulate the detector response. [20] In MCNP, the Surface Card and Cell Card need to be defined to build the geometry of the radiation detector and the source. The material information of the structure will be included in the Material Card for particle scattering calculation. The Source Card is used to define the energy and distribution of the radiation being simulated, in this case, photons. The Tally Specification Card is used to extract the calculation result we are interested in. In this research project, we used the standard F8 Pulse Height Tally to simulate the detector response. This tally records the interaction events in the volume of interest and tracks the secondary particles to the default cutoff energy of 1 keV. The normalized frequency of the deposited energies is output into each energy bin. By simulating the emitted photons

in the detector crystal, we can generate a frequency vs. energy graph, which is comparable to the gamma spectrum obtained from the Multichannel Analyzer (MCA).

3.2 Detector Geometry and Algorithm Validation

To develop an MCNP detector model based on the manufacturer information, we need to validate that the building algorithm shows a good imitation of the structure. Fortunately, Dr. Soo Hyun Byun was able to provide EGS5-simulated efficiency data on an HPGe detector model[21], which can be compared with my MCNP-based simulation result.

The detector simulated is a P-type coaxial HPGe detector manufactured by Ortec. The 69.7 mm diameter × 85.4 mm length germanium crystal is mounted on the aluminum wall, and the detector head is encapsulated in the magnesium end cap. The MCNP model on the detector is shown in [Figure 14](#). The dark blue color germanium cell is built by combining a cylindrical structure and a torus structure. The torus provides a curved edge at the end to imitate the true crystal shape. [22] The center hole (Cell 2) is built with a cylinder and a sphere. The green aluminum cap (Cell 3) and the red magnesium end cap (Cell 5) are built using plane and cylinder surfaces. The outside of the detector material is set to be air, while the interior space of the detector is set to be vacuum. There is also a 30-um thick mylar layer on the top of the crystal for insulation. The material card of mylar is composed as:

Mylar (boPET) [1.38 g/cm³]

H 0.363632

C 0.454552

O 0.181816

The simulated detector has a 1.5 mm internal deadlayer, which is at the outer surface of the Ge crystal for a P-type detector. In the model, the crystal is split into two separate cells, where Cell 1 is the deadlayer and Cell 21 is the active volume.

In the simulation, the F8 tally for only Cell 21 is run to imitate the detector response, as Cell 1 will attenuate and reduce active volume like a deadlayer. In the source card, a point source emitting 661.66 keV photons is placed 25 cm away from the center line of the detector surface. The source emits isotopically, so that the F8 tally output at the 661-662 keV energy bin represents the absolute peak efficiency for the source. Usually, the energy range between output bins will be precise to every 1 keV or even 0.5 keV to ensure the overlap of the count at each energy is minimized. For example, the simulation output for the 661.66 keV response will be divided into 700 channels with 699 intervals, or 1400 channels with 1399 intervals.

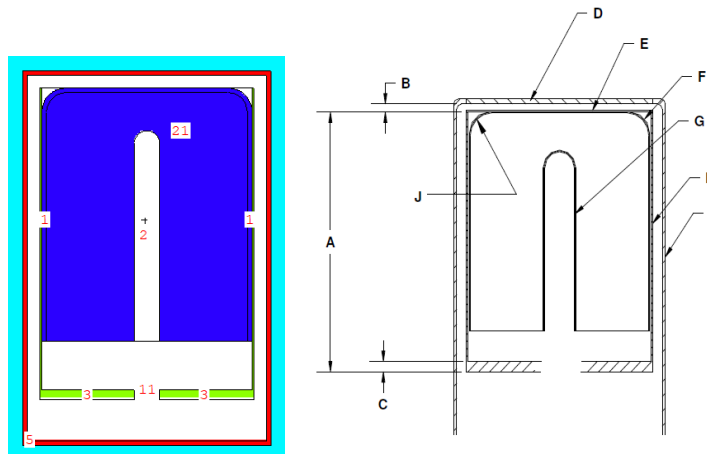


Figure 14: The Ortec SN40P HPGe detector model built in MCNP6.2. The image is the detector structure on the x-z plane. The Ge crystal is displayed in dark blue color with Cell 1 as inactive volume (deadlayer) and Cell 21 as the active volume for detection.

To generate an energy efficiency curve, 40 energies ranging from 53.161 keV to 1951.2 keV are simulated. 1E9 particles are run in each simulation to keep the statistical uncertainty below 0.2%. The efficiency curves generated by EGS5 and MCNP6.2 are shown in [Figure 15](#). Comparing the two curves, the EGS5 simulated values are 0.1% to 13.7% higher than the MCNP result. The efficiency at a low energy range (0-500 keV) has a greater difference (>2%), but the difference converges as the energy increases. For energy greater than 1000 keV, the differences are within 1%. This could be caused by the fine details of the shielding material design. For example, the material in between the source and the detector surface is set to be air with a density of 1.205E-3 g/cm³ in MCNP, but it is not specified in the EGS5 result. If the EGS5 uses vacuum or lower-density air as the material, there will be less attenuation for the incoming energy, especially for lower-energy photons.

This might explain the decreasing difference as the energy increases. Regardless, the near congruence of the efficiency curves indicates that the MCNP building algorithm is replicable for other geometries.

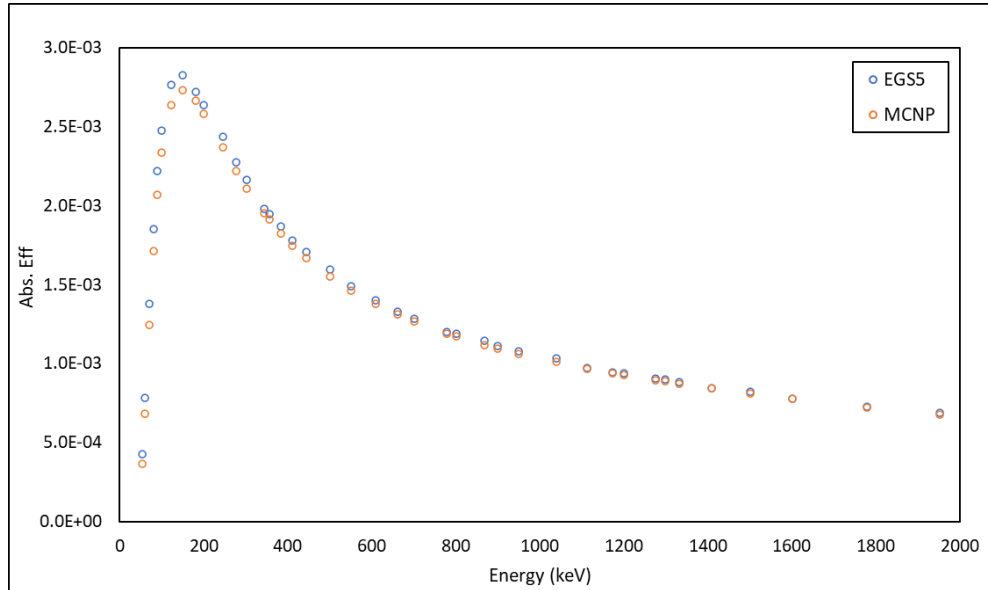


Figure 15: The SN40-P HPGe detector energy efficiency curve simulated by EGS5 (blue) and MCNP6.2 (orange). $1E9$ particles are simulated to ensure the statistical uncertainty is within 0.12%.

Using the same algorithm, I built the MCNP model for the GMX 25-N detector used for this research, which is shown in [Figure 16](#). Detailed detector information can be found in [Chapter 2](#). Other than the geometry and the material difference, a 700-micron lithium contact layer (Cell 2) and a 2.66 mm inner deadlayer (Cell 8) is added to this model.

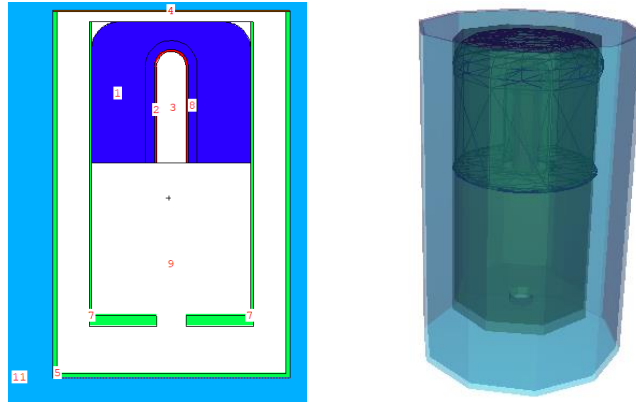


Figure 16: The Ortec GMX 25-N coaxial HPGe detector on the x-z plane (left) and the 3D structure of the detector (right) with the Ge crystal displayed in wireframe.

3.3 Deadlayer Thickness Estimation

Unlike the P-type detector above, this N-type detector has the deadlayer at the inner surface of the Ge crystal, which is the reason why the N-type detector has higher efficiency than the P-type for low energy photons. Since the manufacturer did not provide any information about the total active volume, the thickness of the deadlayer needs to be determined through simulation. The manufacturing data sheet stated that the relative efficiency at 1.33 MeV is measured to be 14.4%. This value is relative to the efficiency of a 3'x3' NaI detector at 25 cm, which is 1.2E-3. [23] Therefore, the expected absolute efficiency of the 1.33 MeV point source at 25 cm from the HPGe detector is calculated to be 1.728E-4 using the equation:

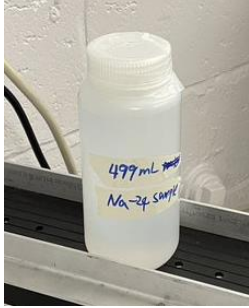
$$Rel. Eff = \frac{Abs. Eff \text{ at } 25 \text{ cm}}{1.2 \times 10^{-3}}$$

Then, the MCNP geometries with different thicknesses of the inner deadlayer are built to test the efficiency of the active volume using the F8 tally. The simulation result shows that the deadlayer thickness of 2.66 ± 0.01 mm in the model will provide absolute efficiency of $1.728E-4$. Based on this result, the HPGe model with the 2.66 mm deadlayer thickness is used in the incoming research process. The comparison between this model and the experimental result of calibrated sources will be discussed in Chapter 4.

3.4 Source Geometry and Distribution

Table 5: The geometries for the sources

Source	Picture	Geometry	Case material	Filling Material
Point Sources		4.75 mm active diameter	plastic	Epoxy
Disk sources		50.8 mm diameter	Stainless steel backing	N/A

Na-24 volume source		7.2 cm diameter x 14 cm height	Plastic	Water
Marinelli beaker		8.3 cm hole diameter, 7.5 cm hole depth 19 cm diameter, 18.1 cm height	Plastic	1g/cc epoxy
1 Quart Plastic waste container		4.5" top diameter, 3.948" bottom diameter, 4.773" height	plastic	Contaminated masslin cloths
Non-processible waste container		182.88 cm x 119.38 cm x 102.39 cm (LxWxH), 0.28 cm thick	Stainless steel	Filling waste materials

As mentioned previously, several source cards are built on MCNP for validation and research purposes. The original geometries for the sources are listed in [Table 5](#). In MCNP modeling, the disk source is built using the RCC macrobody structure with activities distributed in a very thin (0.1mm) layer at the surface of the disk. For the Na-24 volume source, the 500 mL bottle structure is simplified into a right cylinder

with the same diameter but a shorter height, as the solution does not fill the top of the bottle. The Marinelli beaker is built using two right cylinder geometry with filling material of IPL epoxy matrix based on the PNNL-15870 report [24].

The 1-quart plastic container structure is built as a truncated right-angle cone shape using the TRC macrobody structure. The filling material is set as rayon to represent masslin cloths, and the density is input based on the actual mass of the sample. The blue waste container is built with a simple rectangular box structure with a 0.28 cm thick wall. The material of the container is built based on the stainless-steel composition and density provided by LEP ([Figure 17](#)).

The MCNP material card information for the compound materials used in the source building is summarized in [Table 6](#). The activities are evenly distributed throughout the source volume (surface) for all the models. In addition, the “hotspot” distribution is also applied to the blue waste container model in the research of the location information for unevenly distributed wastes. This experiment will be further discussed in [Chapter 5](#).

Table 2: Material Composition of Stainless Steel for LLW Bins [1]

Constituent	Weight Percent (%)	Density (g/cm ³)
Carbon	0.08	7.85
Silicon	0.75	
Manganese	2	
Phosphorus	0.045	
Sulfur	0.03	
Nickel	12	
Chromium	20	
Nitrogen	0.1	
Iron	64.995	

Figure 17: LLW bins' material composition

Table 6: MCNP material card design for measured sources

Source material	Marinelli Epoxy Matrix	Uline 1-quart container (HDPE)	Masslin Cloths (rayon)	LLW Bin (stainless steel)
Chemical Formula	C ₂₁ H ₂₅ ClO ₅	C ₂ H ₄	C ₆ H ₁₀ O ₅	N/A
Density (g/cm³)	1	0.94	Varies by sample	7.85
Material Card	6000. 21 1000. 25 17000. 1 8000. 5	1000. -0.143724 6000. -0.856276	1000. -0.062167 6000. -0.444452 8000. -0.493381	6000. -0.08 14000. -0.75 25000. -2 15000. -0.045 16000. -0.03 28000. -12 24000. -20 7000. -0.1 26000. -64.995

3.5 Multi-Detector Array Design

Since the LLW waste container has a much greater volume compared to the other source samples measured in the lab, one detector is not sufficient to acquire source

term information. As a result, multiple MCNP models are developed to simulate the response when different detectors array is used for source measurement. [Table 7](#) summarizes the detector arrays developed during the research and the source distribution used for the array. Two sets of arrays are developed for different purposes: the homogeneous waste model has an evenly distributed source inside the container, which is used to compare the efficiency of different detector geometry; while the hotspot model has a source of 10x10x10 cm size distributed at different locations in the waste container, which is used to compare detector response for contamination at different positions. The detail of the source distribution and the simulation outcome of each design will be explained thoroughly in [Chapter 5](#).

Table 7: The detector array design on waste container measurement

Array Design	Number of Detectors	Number of Surfaces Occupied	Array Pattern Description	Waste Distribution Pattern
1d1s	1	1	Center of the front surface	Homogenous
4d1s	4	1	4 at the center of the front surface	
4d4s	4	4	1 on each of the sides	
5d1s	5	1	5 at the center of the front surface	
5d5s	5	5	1 one each of the sides and 1 on the top surface	
7d1s	7	1	7 at the center of the front surface	
8d4s	8	4	3 on the front and back, 1 on the left and right	
3d3s	3	3	A detector on the front, right, top of the container	Hot Spots
3-detector array	9	3	3 detectors diagonally on each of the surfaces	

To ensure the geometry of the detectors is consistent, the input card of the universe (U), fill (FILL), and TRCL is applied to duplicate the original HPGe structure. To perform this, an empty cylindrical cell is created that includes all the detector's cells (Cell 1-9) and set to fill=1. Then, we can move each detector cell into this structure by adding u=1 at the end of each line of Cell 1-9. The TRCL parameter can then be applied to the empty cylinder cell to duplicate the structure, as well as perform displacement and rotation. In this situation, if the F8 tally is run on Cell 1 (HPGe crystal), the pulse height information from all the Cell 1 duplicated structures will be summed up as one value. This means that we will obtain the efficiency information for all the HPGe crystals together. If we want to obtain the signal from each detector separately, we will need to define new cells with the same structures as the original cells but belonging to another universe (i.e., u=2). By defining a new empty cell with fill=2, a separated detector structure will be created. Then, the F8 tally of each cell can be run individually to acquire detector response separately. The F8, F18, and F18 tallies of the three Ge crystals are acquired to collect the detector response separately. For example, the tally card used for the three-detector model is F8:p 1, F18:p 21, and F28:p 31.

3.6 LaBr3 Detector

The 2"x2" LaBr3 detector structure is relatively simpler than the HPGe detector, as the crystal is cylindrically shaped rather than the coaxial shape of Germanium. The

modeled structure consists of the center active volume and a 1mm thick aluminum case, with an internal gap filled with air (Figure 5). Without structures of the PMT and the bulky part of the case, this geometry is simplified compared to the model built by R. GARNETT [25] and A. LARANJEIRO [17]. However, the simulation result is comparable to the two models mentioned above. As shown in Table 4, the peak efficiency from my model is within a 5% difference compared to the other two models, which is acceptable considering the slight variation in source distance for each model. Moreover, this geometry is built for the purpose of the multi-detector response model for waste container measurement, where the peak efficiencies are compared for the same structure at different positions. Therefore, this model will be acceptable as long as the active volume response is correctly simulated.

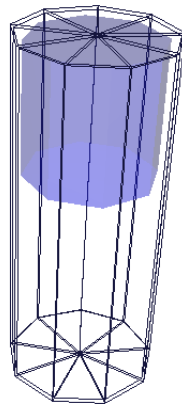


Figure 18: The MCNP 3D structure of the LaBr3 detector. The crystal is coloured in blue, and the 1mm thick Al case is displayed in wireframe.

Table 8: Comparison of the Simulated Absolute Peak Efficiency of a Co-60 Point Source at 20cm

Author	MC Code	1173 keV Peak	1332 keV Peak
Garnett	GEANT4	8.20E-04	7.20E-04
Laranjeiro	MCNP6	8.30E-04	7.60E-04
Zhou	MCNP6.2	8.35E-04	7.48E-04

In terms of the multidetector model for the LaBr3 detector, the 3-detector model is also built for hotspot measurement. Since the geometry for the detector is much simpler than the HPGe detector, the Universe and Fill function is not used in this model. The geometries of three separate detectors are directly coded at three positions relative to the container. Three F8 tallies are run for the three LaBr3 crystal structures to acquire detector response.

Chapter 4: Simulation Accuracy Validation

4.1 Detector Efficiency Test with Point and Disk Sources

After establishing the MCNP model, I used standard calibration sources to verify the accuracy of the simulation. The source-to-detector distance was set at 25 cm to eliminate the true coincidence summing (TCS) effect of the multi-photon emitters. As the distance increases, the detection efficiency decreases, which reduces the chance of coincidence. The decreasing efficiency will result in a lower count rate, which is also good for eliminating the pile-up effect.[26] Conversely, the decreasing efficiency needs to be compensated with extended counting time to ensure 10,000 counts on the main peaks.

For the convenience of the efficiency comparison, an energy efficiency curve for a point source at 25 cm is first constructed with 41 energies. Each energy is simulated separately with 1E10 particles to ensure the statistic uncertainty is less than 0.1%. the efficiency curve is shown in [Figure 19](#), along with a 4th-order polynomial function fitted in the log scale. The fitted curve demonstrates high consistency following the function with an R-square value of 0.9994.

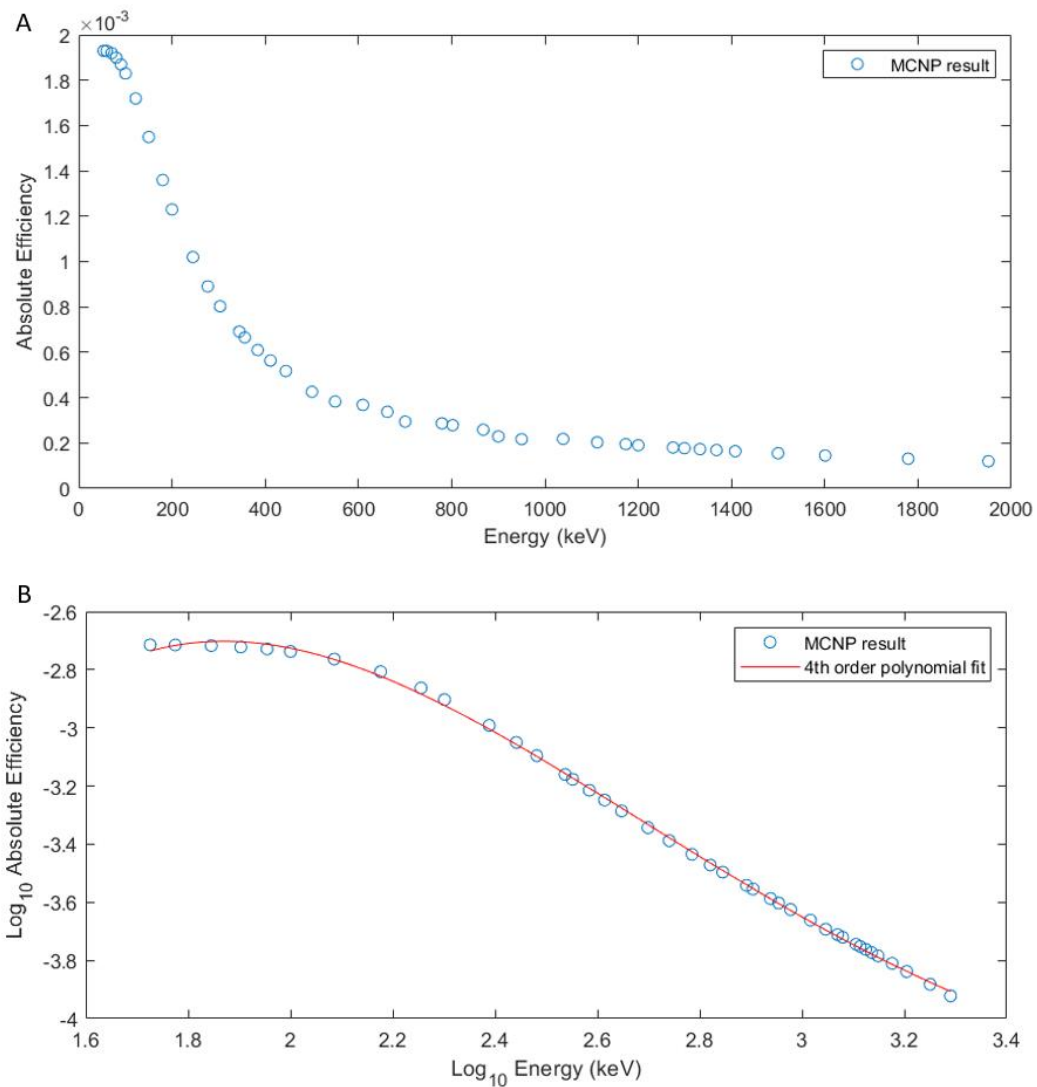


Figure 19: The energy efficiency curve for point sources at 25 cm (A) and the curve fitting result in log-log scale (B).

The MCNP simulated energy efficiency and the experimental measurement for the Eu-152 and Cs-137 point sources are plotted in [Figure 20](#). The Eu-152 source was counted for 24 hours, and the Cs-137 source was counted for 1.5 hours to ensure the

major energy peaks recorded more than 10,000 counts. The experimental absolute efficiency is calculated through Equation (1) below:

$$Abs. Eff = \frac{Peak Area}{Source Activity \times Counting time \times Emission Probability} \quad (1)$$

In the plot, the experimental efficiency curve follows the general trend as they decrease with increasing energy. However, there is a significant difference between experimental and simulation results, from 7% to 21%. As the energy increases, the difference between the simulated result and the experimental result decreases. For photon energies greater than 500 keV, the difference between the experimental value and simulated result is less than 15%. The measured data is also fitted with the 4th-order polynomial in Figure 19B and results in a good fit with an R-squared value of 0.995. However, the experimental results appear to be lower than the simulated results. This could be caused by the additional attenuation from the measurement setup, or by the uncertainty for the source position. Based on this comparison, the MCNP model demonstrates reasonable estimation for the efficiencies relative to different energy. However, it does not provide a good estimation of the actual detector response (absolute efficiency).

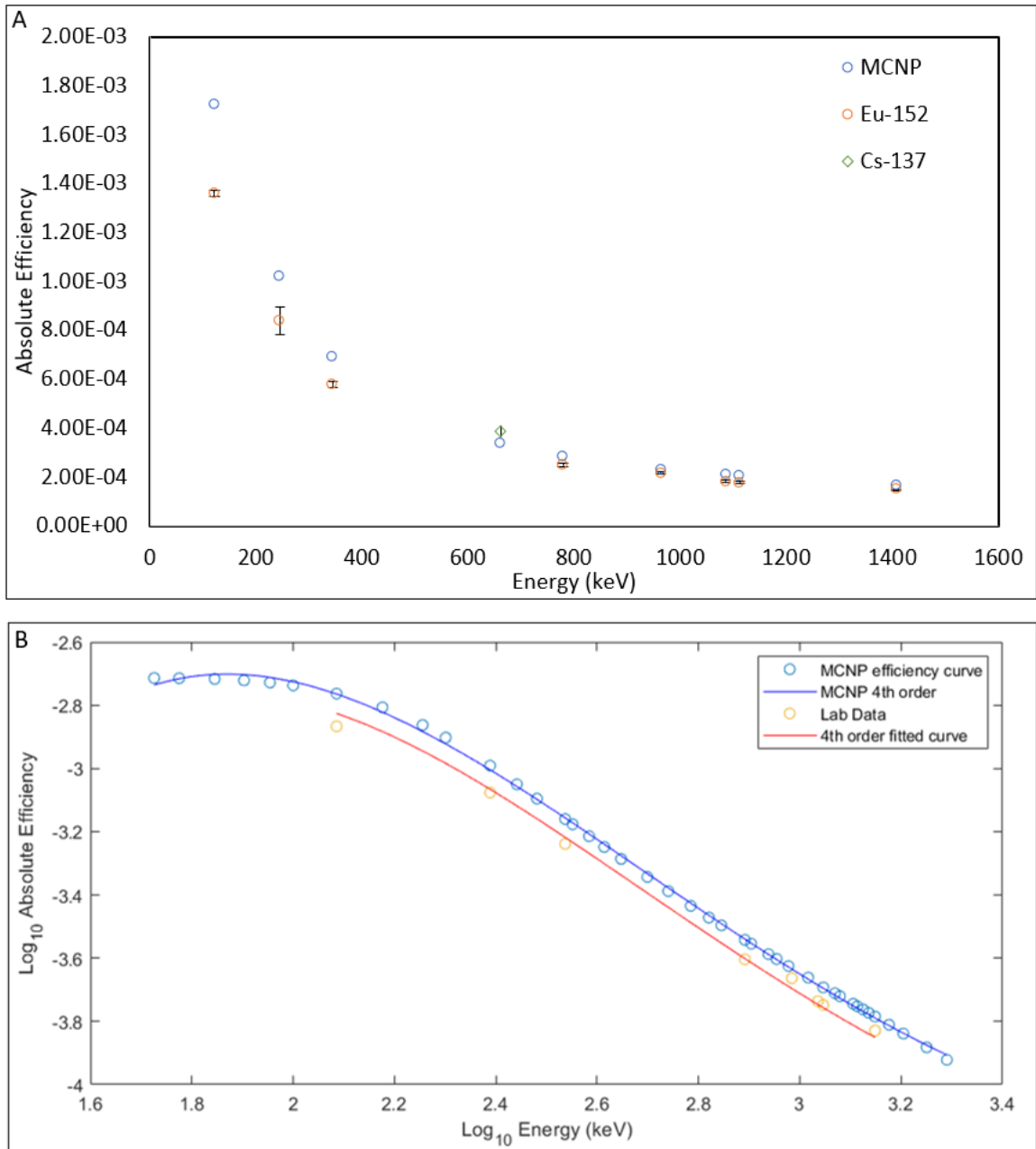


Figure 20: Point source measurement at 25 cm using Eu-152 and Cs-137 (A), and the comparison of Eu-152 energy result with the MCNP simulated efficiency curve in log scale (B).

Since the complex decay mode for Eu-152 can introduce uncertainty to the analysis process, another experiment with more energy variation is performed using disk sources. As mentioned previously in **Chapter 2**, the disk source is placed parallel to the detector surface for measurement. The mixed-Eu source contains Eu-152, Eu-154, and Eu-155, which provides a wide range of photon energy for analysis. In contrast, the Co-60 source emits two photons with high emission probability, which provides high accuracy for the analysis. The Eu source is counted for 26 hours, and the Co source is counted for 15 hours.

The analysis result is plotted in Figure 21. With more data points available, a smoother energy efficiency curve can be observed for the experimental result. Compared to the MCNP result, we still observed a bigger disagreement at the lower energy range (<500 keV) with a 14% to 33% difference. This could be caused by the high level of background noise from the long counting time, as well as the coincidence summing and pile-up effect for the complex decay process of the Eu source. As energy increases, the difference between them converges to be as low as 1%. The two Co-60 peaks have the two highest correlations with the simulation as the relative difference for the 1173 keV and 1332 keV peaks are 1.47 % and 0.1%, respectively. This could be caused by the simpler decay scheme for the Co-60 does

not produce much Compton continuum, which affects the background radiation for the lower energies.

Generally, the trend in disk source measurement is more representative than the point source measurement. This result has demonstrated that my MCNP model of this HPGe detector is reliable in measuring small sources.

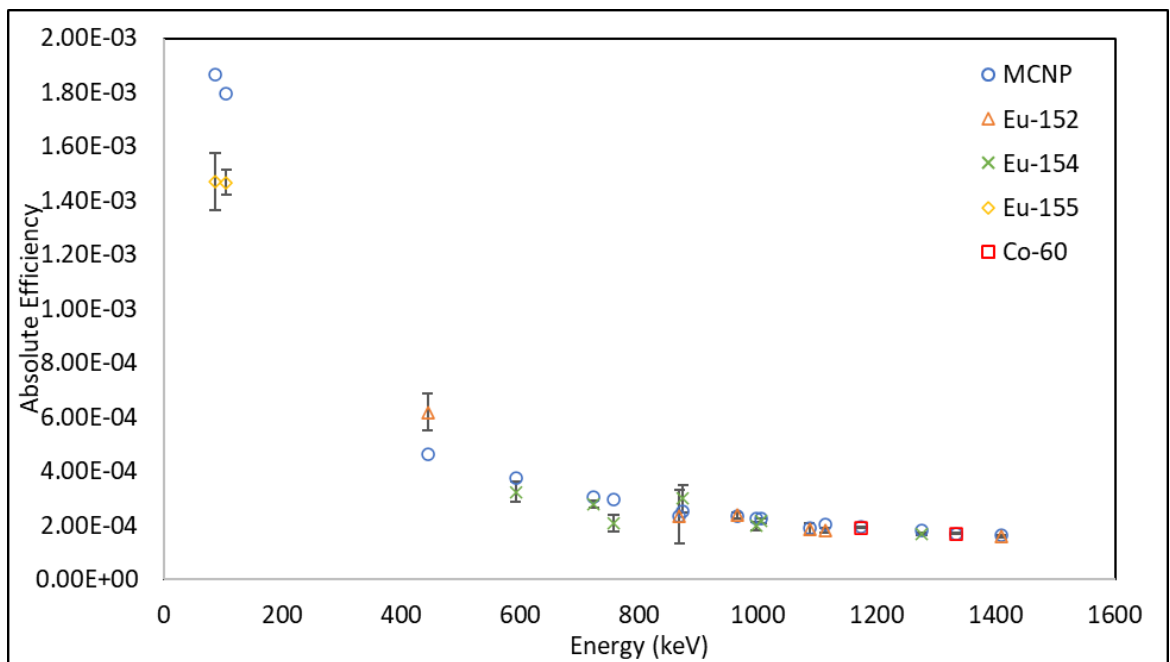


Figure 21: Disk source measured efficiency and simulated efficiency (blue) at 25 cm. The uncertainty for the MCNP result and the experimental result is within 0.1%.

4.2 Detector Efficiency Test with Volume Sources

Since our final goal is to develop calibration techniques for samples as large as the industrial waste container, this detector model needs to be tested with volumetric

samples for validation. In this experiment, we measured a calibrated 4L Marinelli beaker source and a neutron-irradiated 500 mL Na-24 solution.

The 4L Marinelli beaker contains Eu-154, Eu-155, and Sb-125 with the activity of 17000 ± 500 Bq, 5400 ± 200 Bq, and 5000 ± 200 Bq, respectively, on the date of measurement. This source composition is great for energy calibration due to its wide energy range coverage. Eu-155 emits low-energy photons ranging from 26.527 keV to 105.3 keV. Sb-125's gamma emission is in the range of 300 to 700 keV, which covers the medium energy spectrum. Eu-154 emits a wide range of photons with the majority of energy in 700 to 1400 keV, which greatly covers the higher energy range. Twelve energies with emission probabilities greater than 10% are chosen to be analyzed and simulated.

The simple MCNP geometry model is designed and shown in [Figure 22](#). The material and the thickness of the beaker wall are not included, and the filling material is set as an IPL epoxy matrix. In the experiment, the beaker is placed 25 cm from the detector surface to minimize the effect of coincidence summing from the multiple-photon emitters. The hole of the beaker faces the detector with the center lined up. An efficiency curve was generated using the 12 simulated energy and will be used for comparison.

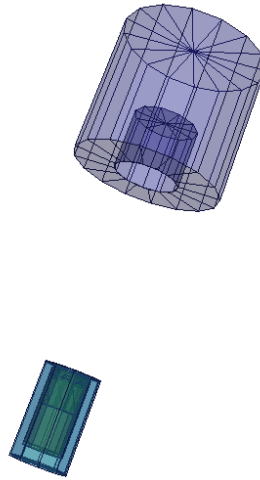


Figure 22: The 3D structure of the setup in MCNP. The blue volume on top is the Marinelli beaker, while the bottom structure is the HPGe detector. The near-surface of the beaker is 25 cm from the detector surface.

After a 24-hour count, 8 of the photon peaks can collect a peak area greater than 10,000 counts, while the other 3 peaks from the Sb-125 emission line can only collect more than 5000 counts. The absolute efficiency of these energies is calculated using the count rate information and compared with the simulated efficiency curve, which can be seen in [Figure 23](#). In this comparison, we observed a similar trend as the previous testing with disk and point source, where the difference at low energy region is very distinct but converges as energy increases. The first five photons with energy below 500 keV have a difference from 0.7% to 35.5%, while the rest can be as low as 1.5%. This trend is similar to what we observed from the previous experiments, where the spectrum analysis for low-energy photons is still a challenge. Moreover, we can still observe a relatively smooth curve from the experimental data

similar to the point source and disk source measurement. This indicates the MCNP detector model works consistently regarding the source geometry.

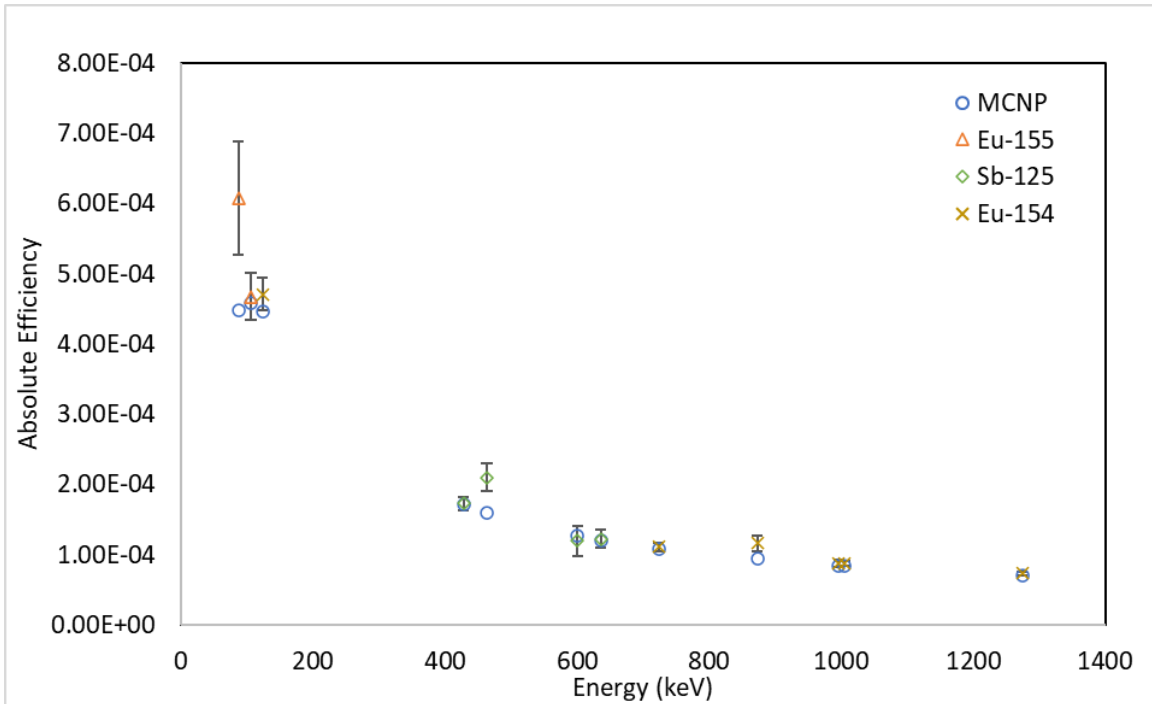


Figure 23: Experimental efficiency and simulated efficiency for the 4 L Marinelli beaker. The MCNP simulated result has an uncertainty less than 0.1%.

To test the current detector model accuracy on volume source, a measurement on the Marinelli beaker using the LabSOCS software is performed by the Health Physics group for comparison. The geometry used in the software has the same dimension as the MCNP model, and a 2000-second measurement at a 75 mm distance is performed. The activities of the three radioisotopes can be predicted through the LabSOCS algorithm and displayed in the Interference Corrected Report. The MCNP predicted activity is calculated using the equation:

$$Activity = \frac{Experimental\ peak\ count\ rate}{Emission\ probability \times MCNP\ simulated\ abs.\ efficiency} \quad (2)$$

Since the three radioisotopes are multi-gamma emitters, the activity is predicted for each peak, and the mean is taken to calculate the final activity. The values of the expected activity, MCNP predicted activity, and the LabSOCS predicted activity are displayed in [Figure 24](#). Despite overestimation, the MCNP algorithm appears to be more accurate than the LabSOCS prediction. Compared to the expected activities, the MCNP estimations are 7%-19% higher than the expected activity, while the LabSOCS estimations are 18%-30% lower than the expected activity. The prediction of the Eu-155 activity is the most inaccurate from the MCNP algorithm. This could be from the inaccurate gamma spectrum at a lower energy range. Since the main photons emitted from Eu-155 are 86.5 keV, and 105.3 keV, the overestimated efficiency at the low-energy range will result in an overestimated activity. For the LabSOCS result, the underestimation can be caused by the inaccuracy of the geometry design, or the inefficient counting time. Due to the peak fitting of Matlab, the estimated activities have higher uncertainty compared to the LabSOCS software. However, the MCNP algorithm still has a better prediction of activity out of the 2 methods. If the low energy range efficiency can be corrected for the MCNP detector model, I believe this MCNP-based method can outperform the LabSOCS software on complex geometric source measurements.

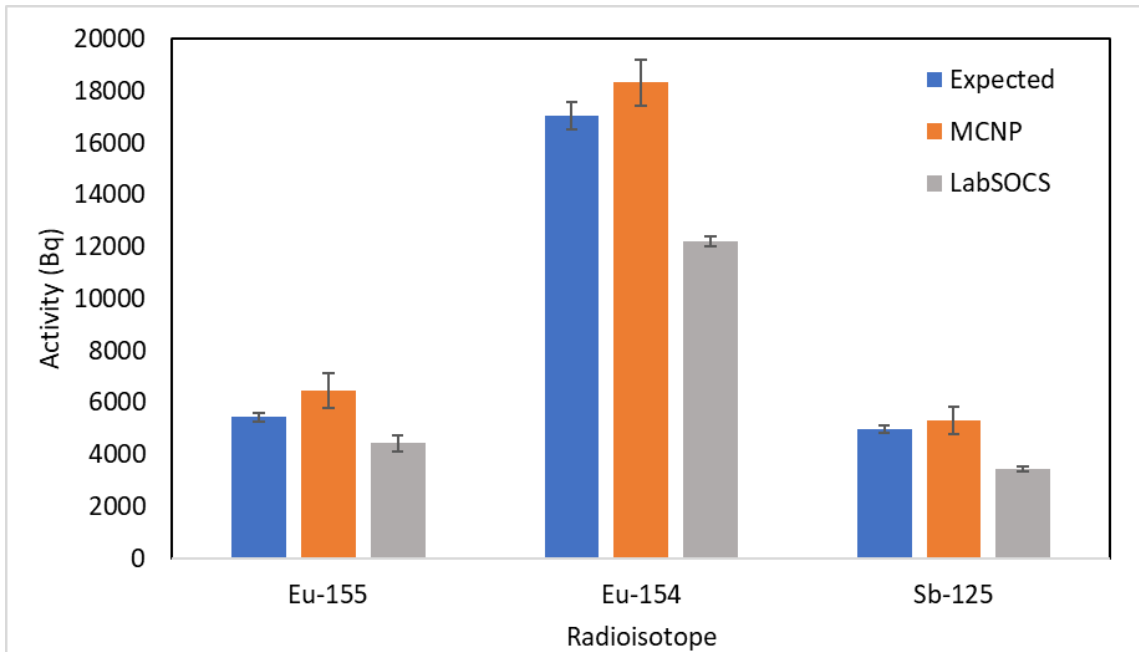


Figure 24: The expected activity of Eu-154, Eu-155, and Sb-125 in the Marinelli beaker compared with the activity predicted using the MCNP algorithm and LabSOCS software.

An additional experiment was also performed using a self-made Na-24 volume source. The idea behind this is to produce a volumetric source with a simpler geometry and emission spectrum to minimize the data uncertainty. Na-24 can be easily produced through neutron activation with help from the McMaster Nuclear Reactor. After dissolving 0.0456 g of NaNO_3 powder into 1 mL of distilled water, a 10-second irradiation is performed on the sample to produce Na-24. Na-24 emits 1368 keV and 2754 keV of photons with probabilities of 99.9936% and 99.855%. The activated solution is measured at 25 cm using the HPGe detector to acquire the peak count rate for the 1368 keV peak. Since our previous testing has already shown the MCNP model has high accuracy for high-energy photons, the activity can be

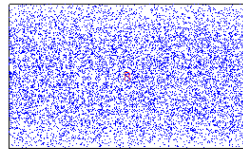
estimated using Equation (2). Due to the relatively short half-life of Na-24 (15 hours), decay correction needs to be applied to the count rate result using Equation (3):

$$f = \frac{N}{\Delta t} \times \frac{\lambda \Delta t}{1 - e^{-\lambda \Delta t}} \quad (3)$$

where f is the correction rate (s^{-1}), N is the number of disintegrations, Δt is the counting duration, and λ is the radioactive half-life.

Using the equation, the activity of Na-24 after irradiation is estimated to be 56500 ± 200 Bq. The 1 mL solution is then mixed with the 499 mL water to form a 500 mL volume source. This can be performed after the activity decayed below 1000 Bq following Health Physics regulations. Therefore, the ideal time to measure the volume source is at an activity of 1000 Bq. However, due to unforeseen circumstances, the sample transfer was performed 2 days late, which left only 200 ± 1 Bq of activity for us to measure. The 500 mL volume source is measured at 15 cm from the detector. This distance is measured from the detector surface to the base centerline of the bottle. The corresponding MCNP geometry is built and shown in Figure 25. A 24-hour measurement was then performed using our HPGe detector system to acquire as many counts as possible, followed by two measurements using LabSOCS calibrated HPGe detection system performed by health physics. A cylinder source was built on LabSOCS with the same dimension used in MCNP to run the simulation. From the counting result, the initial activity is then predicted using my

MCNP absolute efficiency and LabSOCS algorithm to compare with the expected activity from the decay calculation. The results are listed in [Table 9](#).



11

+

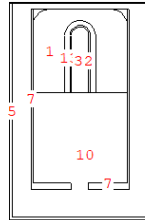


Figure 25: The MCNP geometry for the detector and the 500 mL Na-24 volume sample (cell 8) with source particles displayed. In reality, the setting is horizontal, where the bottle will be placed upright on the measuring stand.

Table 9: Na-24 Volume Sample Activity Prediction with Various System

Measuring System	Source to Sample Distance	Counting Time (s)	Expected Activity at the Beginning of Counting (Bq)	Predicted Activity at the Beginning of Counting (Bq)
HPGe + MCNP	15cm	86400	200.4 ± 0.7	193 ± 16
LabSOCS	9mm	4453.8	65.6 ± 0.3	65 ± 3
LabSOCS	9mm	67919	61.8 ± 0.3	60 ± 3

As shown in the table, the LabSOCS software prediction shows high accuracy, as the predicted value is within the range of the expected value. On the other hand, the estimation result using my MCNP model is approximately 3.5% less than the expected activity. However, the greater uncertainty makes the actual activity land in the range of prediction.

Since the source is measured at a 15 cm distance, true coincidence summing (TCS) might be significant in the measurement. For a point source emitting two photon energies when it decays, the coincidence summing correction (CSC) factor for the photon i can be calculated using the following:

$$CSF_i = \frac{1}{1 - \frac{p_j}{p_i} \varepsilon_{t,j}} \quad (4)$$

Where p is the emission probability of the photon, $\varepsilon_{t,j}$ is the total efficiency of photon j .

A computational-based coincidence summing correction method shown in Sima and Arnold's publication [27] was used to estimate the correction factor. The equation to calculate the effective total efficiency for the photon i is shown as follows:

$$\varepsilon_T^{eff}(E_j, E_i) = \frac{\int_V \varepsilon(E_i, \vec{r}) \varepsilon_T(E_j, \vec{r}) dV}{\int_V \varepsilon(E_i, \vec{r}) dV} \quad (5)$$

where $\varepsilon(E_i, \vec{r})$ is the full energy peak efficiency for photon i at position \vec{r} , and $\varepsilon_T(E_j, \vec{r})$ is the total detection efficiency for photon j at position \vec{r} .

Experimentally, the integral can be performed by performing point source simulation at various positions in the volume and summing them up. In my simulation, I placed the point source at 26 different positions in the geometry. Based on the radial distribution of the cylindrical volume, the number of samples increases as the radius increases to ensure the simulation is a good representation of the actual source distribution. Using the simulation result, the effective total efficiency for the 1368 keV photon of Na-24 is calculated to be $5.73\text{E-}3$, which leads to the CSC factor of 1.006. This value indicates that the TCS effect for the 500 mL Na-24 source at 15 cm is negligible.

The above results show that the approximation for the Na-24 volume sample using the MCNP algorithm is less accurate than the LabSOCS. Many factors might have caused the error in the approximation, but one of the most likely reasons is the weak source activity during the spectrum collection. As mentioned before, the activity for the Na-24 source is around 200 Bq. After dilution and placement at 15 cm, the net peak area for a 24-hour collection is only 3500 ± 300 counts. This value is even lower than the area for the 1460 keV peak produced by K-40 (42400 ± 300) from the background. The long counting time and the short half-life of the Na-24 sample increase its sensitivity to the background radiation, which introduces more uncertainties in the analysis. This experiment could be improved by performing the liquid transportation immediately after the activity decays to 1000 Bq or by measuring the sample in contact with the detector to maximize the input count rate. Unfortunately, there was not enough time for me to reproduce this experiment.

For the LabSOCS result, despite the measurement being performed after the 24-hour HPGe counting, the 9 mm counting distance and the good algorithm resulted in an accurate activity prediction. This shows that the software is reliable in measuring homogeneous volume samples with simple geometry.

Overall, my assessment is that my MCNP model provides a fair simulation accuracy for the energy range greater than 500 keV. To improve this model, additional adjustments such as a correction factor need to be applied for the lower energy range. However, it is sufficient for this research project as our main radioisotope to focus on is Cs-137, which emits photons at 661 keV. Therefore, I can conduct other research topics using this MCNP model.

4.3 Model Application on the 1-Quart Waste Sample Container

Fortunately, we were able to request some waste samples from the waste segregation site to be analyzed. Since the wastes will be analyzed using the LabSOCS system by the McMaster Health Physics department, it is another good opportunity to compare my MCNP model with the commercialized calibration software.

There are 9 waste samples sent to McMaster University in the Uline 1-quart plastic bucket. They are loose contamination found in waste containers aged from 3 to 30 years, and they are collected on Masslin cloths. Each of the samples has a significant count rate when surveyed with the pancake meter but has no information on

radioisotopes or activity. From the information provided by LEP, Cs-137 is almost always in the presence of reactor by-product. With its long half-life, it should always be present in the waste. Therefore, I decided to focus on quantifying Cs-137 by combining gamma spectrometry and MCNP simulation.

The first step is to build an MCNP model on the waste container. The dimension of the container can be found on the Uline website, and the material information of the masslin is set to be rayon based on the PNNL material report [4]. The average densities of the masslin are calculated to range from 0.10 to 0.22 g/cm³ based on weight measurement. However, the distribution of the activity is unknown since the density of the masslin will not be consistent throughout the volume. Meanwhile, the amount of contamination varies on each cloth. The only information we have is that the cloths tend to be denser at the bottom as they are stuffed in by surveyors, which means we will be expecting a higher count rate from the bottom of the container than the top. In the source model building, I decided not to modify the source distribution parameters but to build two models of source placement. Referring to [Figure 26](#), two models are built with either top or bottom facing the detector to simulate the absolute efficiency of the detector. For each sample, two simulations will be performed with their density to obtain two absolute efficiencies. In the experiment, the samples will be measured in both positions to collect the activity information for the two most extreme cases. Then, by combining the gamma spec information with the simulated efficiency, we can calculate a maximum and minimum value of the activity for prediction using [Equation \(2\)](#). Since Cs-137 will

not have a coincidence summing issue as a single-gamma emitter, I measure the container at 10 cm from the detector to limit the system dead time below 0.4%, which minimizes the pile-up effect from the high count rate.

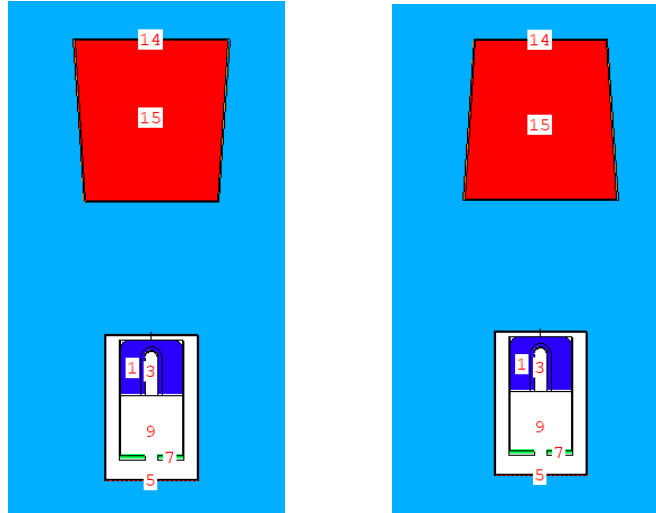


Figure 26: The upright (left) and reversed (right) geometries built on MCNP with the bottom and top of the container facing the detector. The container is 10 cm from the detector. The masslin volume is shown in red inside the container.

The LabSOCS measurement is completed by the McMaster Health Physics Department using an Ortec-calibrated HPGe system. The activity result used for comparison are taken from the Interference Corrected Activity Report, where the decay and coincidence summing of the isotopes are included for the activity estimation. However, this measurement can only assume the uniform distribution of sources inside the geometry. As the bottom of the container faces the detector when counting, the estimated activity will be higher than the actual value due to the higher density at the bottom.

In the ideal case, I would expect that the activity predicted using the upright model will be comparable to the LabSOCS result, while the real activity will be in between the upright and reversed value. In the result presented in [Figure 27](#), the LabSOCS predicted activities for Sample #1,2,3,8,9 are higher than both MCNP predicted models. Comparing the average of the upright and reverse models on each container, the LabSOCS results are 9%-43% greater than the MCNP results. The only samples that satisfy my prediction are Sample #4 and #5, where the LabSOCS result with error bar is in between the two MCNP results. The activity predicted using the LabSOCS algorithm tends to be higher than my MCNP algorithm. This phenomenon is also observed in Pritchard's publication in 2013[28], in which they found that the average efficiency simulated by MCNP on measuring U-235 enriched soil with LaBr detector is 10% higher than the ISOCS simulation. Generally, we cannot conclude whether the software or the MCNP has done a better job since we do not have enough details about the activity and distribution of the masslin filling. Some further experiments can be done by measuring the samples from other different angles on both systems to provide a better estimation.

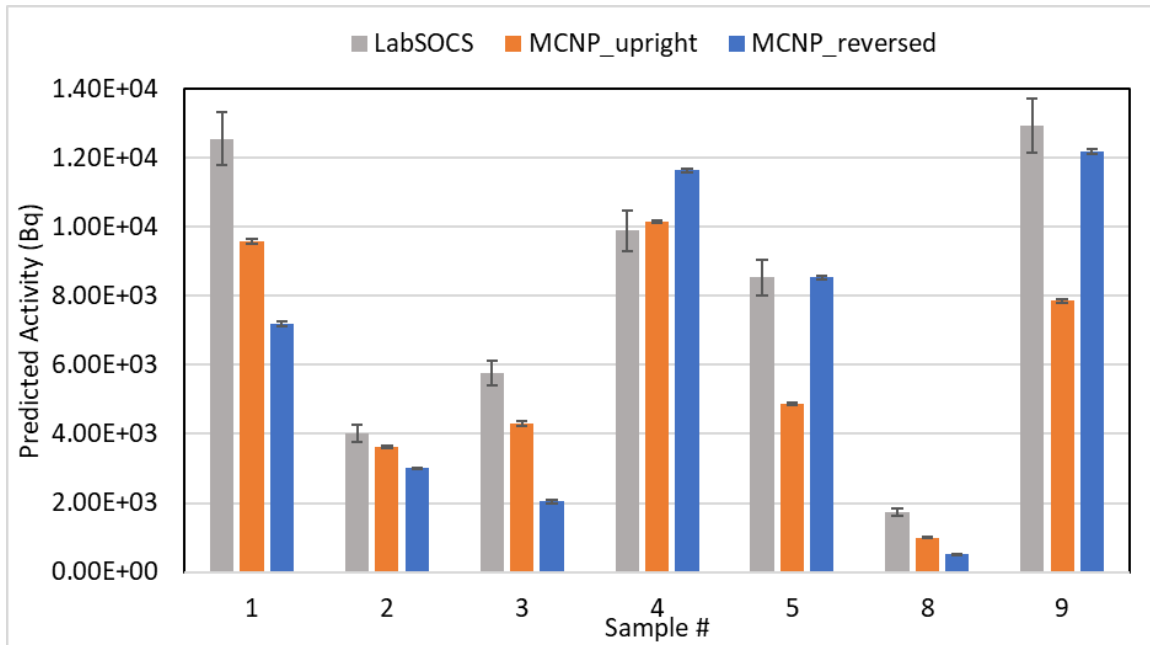


Figure 27: The predicted activity of Cs-137 within each volume sample using three different models. The result for SV6 and SV7 are not included since there is no significant amount of Cs-137 detected in the samples.

Chapter 5: Extensive Study on Volume Source Distribution

5.1 Detector Efficiency Dependence on Volume Geometry

In **Chapter 4**, we established an MCNP model for the HPGe detector and validated its accuracy in the range from 500 keV to 1500 keV. Since the goal of this project is to develop a calibration method to link detector efficiency with industrial-size volumetric sources, we will need to investigate how volume and activity distribution will affect detector output. In this chapter, I build several models of volumetric sources on MCNP and use the F8 tally to simulate the detector response on each case.

The first topic I investigated is the efficiency dependence on the detectors' position arrangement. Since I want to eventually develop a multi-detector system to increase detection efficiency, I need to first investigate if the position of the detectors will affect the measurement.

The first step is to develop a source model for the container based on the non-processible waste container specified in **Chapter 3**. The thickness and the material components of the stainless steel wall are adopted from the OPG's technical basis report[18]. For the convenience of the comparison, the filling material inside the container is set to be liquid water. Two detector distribution styles are modeled. The first one has a different number of detectors placed at the center of the front container surface, where 1, 4, 5, and 7 detectors are placed for testing. An example of the 7-detector model is shown in Figure 28(A). The other distribution style placed

detectors at the center of different surfaces. Three different models are built, including 4 detectors on 4 sides; 5 detectors on 4 sides plus the top surface; as well as 8 detectors with 3 on the front and back surface, plus 2 on the left and right surfaces. An example of 5 detectors on 5 surfaces is shown in [Figure 28\(B\)](#). All the detectors are placed 10 cm from the container wall.

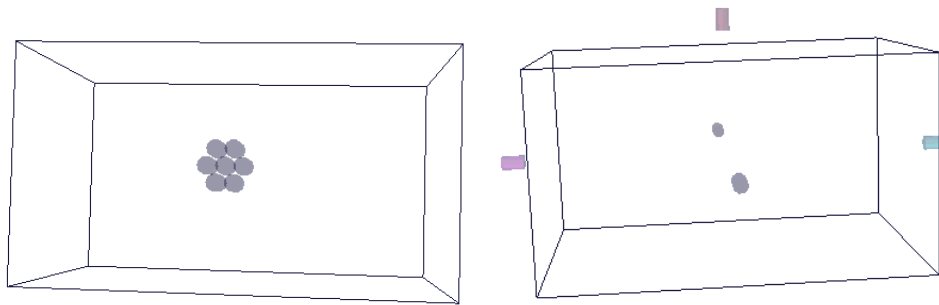


Figure 28: The 3D view of the 7d1s model (A) and the 5d5s model (B)

For this simulation, all the detectors are set to be in the same universe, which means that the F8 tally will treat all the active volumes as one cell. Therefore, the output of this simulation is the combined absolute efficiency of all the detectors. The simulation of 662 keV and 1332 keV photons are run separately, and the output is shown in [Figure 29](#). The general trend shows that more detectors tend to provide higher detection efficiency. When the number of detectors stays the same, the geometry of all detectors at the same surface results in a slightly higher (around 4%) efficiency than distributed to all surfaces. This result makes sense since the container is rectangular shaped so that the photons from the center of the volume need to travel a further distance with more attenuation to reach the detectors on the

left and right sides. It is worth mentioning that the efficiency of the 7d1s is similar to the 8d4s for the 662 keV photons and is even higher than the 8d4s model for the 1332 keV photons. The result from this simulation experiment concludes that the detection efficiency is not always higher for a greater number of detectors. Also, it would be more efficient to place the detectors on the same surface rather than distribute them when measuring an evenly distributed volume of waste.

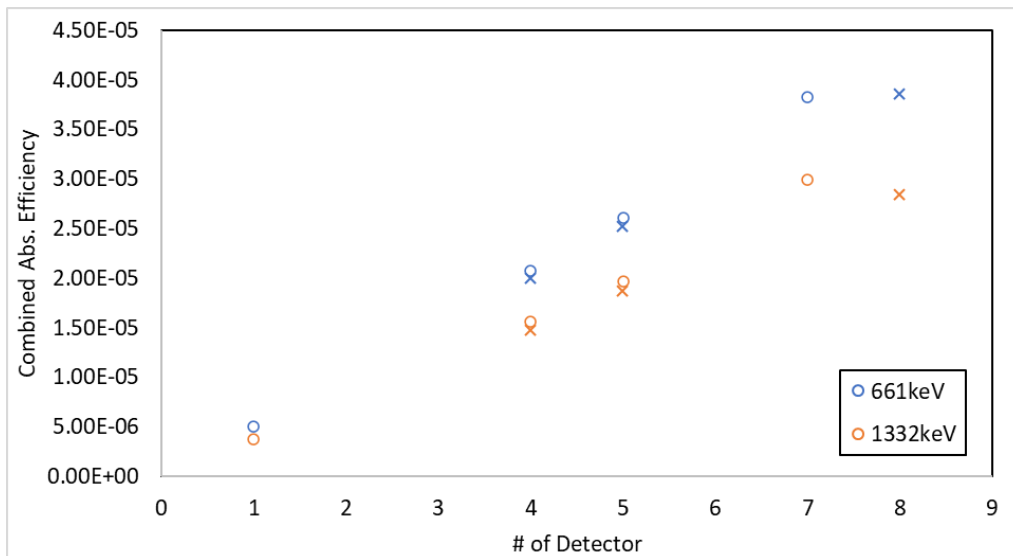


Figure 29: The combined absolute efficiency of different detector distributions. The “o” data points represent the detector geometry at the same surface, while the “x” data points represent the detectors that are distributed on several surfaces. The error bar is not included in this graph, but the simulation is run to ensure the statistical uncertainty is below 0.5%.

5.2 Waste Container Materials Simulation

Another topic to investigate is the MC model of the waste materials in the containers. Regardless of the contamination presented on the wastes, the waste material itself will attenuate the decayed particles, which lowers the detector efficiency. Currently,

the CMSR project sorts the incoming wastes into five waste streams, including non-processible, compactable, metal, incinerable, and denser incinerable wastes. The example of waste materials for each stream is listed in [Table 10](#). With the randomness of the waste materials presented in the CANDU waste, it will be challenging to build a source model that includes all the material information. Therefore, seven groups of material combinations are built to investigate the impact on material atomic number and density. Each group of materials is made up of three commonly found objects from the sorted waste, and they are randomly chosen. The information of the 7 groups is presented in [Table 11](#) with the corresponding density for each sample.

Table 10: CMSR waste streams and the sample materials

Waste Streams	Non-Processible	Compactable	Incinerable (normal and dense)	Metal
Materials Example	battery, charcoal, dirt, Tyvek, RPPE	Filter, plastic bottle, jeans, glass	Wood, paper, masslin, rope, mop	Electronics, screw, chain, saw blade

Table 11: Seven groups of waste combinations with the material information. The PNNL materials used for the material card are shown in brackets.

Waste Group	Material 1	Material 2	Material 3	Average Density (g/cm³)
1	Wood (wood)	Glass (quartz)	Plastic (PET)	1.51
2	Jeans (denim)	Chain (316 stainless steel)	Rubber (natural rubber)	3.47

3	PPE (PE)	Cardboard (cellulose)	Rope (Nylon, Type 11)	1.29
4	Silica gel (SiO ₂)	Metal (iron)	Rubber flooring (Neoprene)	3.92
5	Charcoal (active carbon)	Dirt (earth)	Copper wire (copper)	3.64
6	Rope (polypropylene)	Aluminum foil (aluminum)	Paper (printer paper)	1.43
7	Steel (high carbon steel)	Iron rust (Fe ₂ O ₃)	Aluminum (aluminum)	5.26

The MCNP simulations were run on each waste group, and the absolute efficiencies for the Cs-137 and Co-60 gamma peaks were obtained. [Figure 30](#) shows the relationship between detector peak efficiency and the density of each waste group.

The efficiency relative to the Group 1 efficiency is plotted in the chart, and a trendline is fitted with the power function $y=1.2815x^{-0.89}$ on the 662 keV data.

Despite the inconsistency of the atomic number for each group of material, the fitted function shows a good correlation with the data points with an R² value of 0.9972.

Moreover, the efficiency data for all three photon energies are identical throughout the density range of 1.285 to 5.26 g/cm³, as the difference is less than 2.6%. This result indicates that the detector efficiency tends to be greater affected by the density of the shielding materials rather than the atomic number or type of the materials.

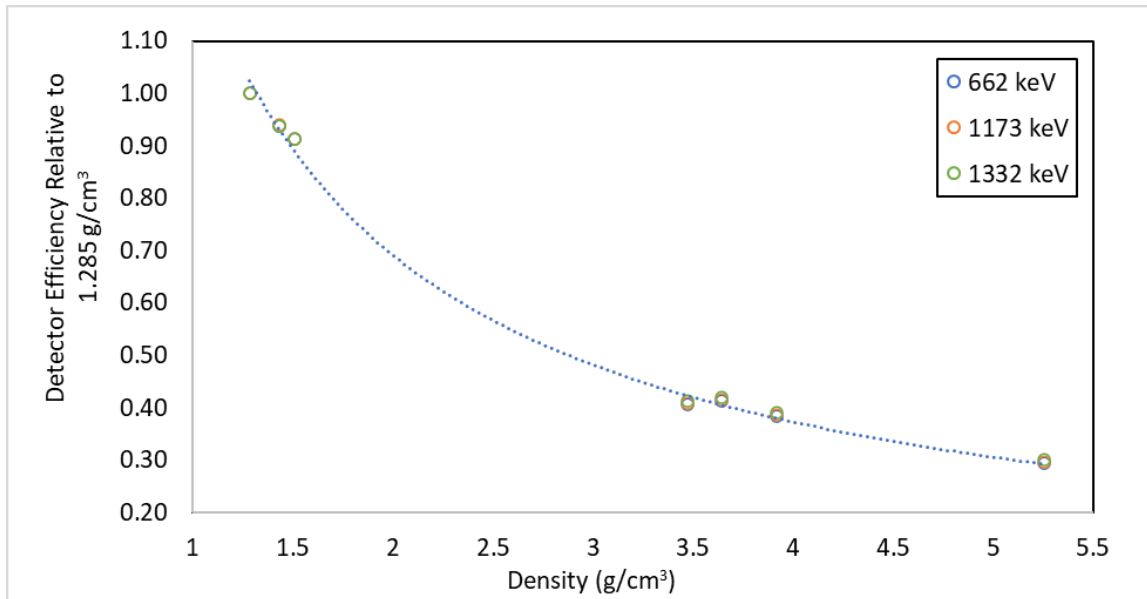


Figure 30: The detector efficiency on 662, 1173, and 1332 keV peaks for different densities of 7 waste compositions relative to Group 1. The blue trendline is a fitted power function for the 662 keV data.

To further test this hypothesis, another study focusing on Group 1 and Group 7 materials is performed. These two groups are chosen due to the drastic differences in their material composition. As Group 1 consists of materials with low atomic numbers, and Group 7 consists of metals with higher atomic numbers. The average atomic number for Group 1 and Group 7 are 7.9 and 19.8, respectively. The simulation is performed on the two groups at different densities to observe the impact on detector efficiency. Seven densities ranging from 0.1 to 0.7 g/cm³ are chosen for the test rather than the 1.3 to 5.3 g/cm³ used in the previous simulation. This is because the wastes do not fully occupied the whole container space, as there will be many air gaps in between to lower the average density. Based on the CMSR

Material Sorting database, the densities of the filled waste inside the containers vary from 0.16-0.69 g/cm³. Therefore, the density of the volume is manually set from 0.1 to 0.7 g/cm³ in the MCNP cell card to use for simulation.

From the simulation result (shown in [Figure 31](#)), we observed that the detector efficiency of 662 keV photons for Group 7 materials is 3% to 7% lower than the Group 1 materials at the same density, despite the 2.5 times difference in their average atomic numbers. However, for every 0.1 g/cm³ increase in density, there is an 11% to 20% decrease in detector response. Similar trends are shown in the 1332 keV photons as well, but with a smaller difference between the two groups due to the better penetrating ability. Based on this discovery, I think it would be better to build my models based on the average density of the filling material rather than the atomic number of the materials. Especially when the weight of each waste container fluctuates so greatly in the sorting site, it would be more conservative to focus on the density of the actual waste during on-site measurements.

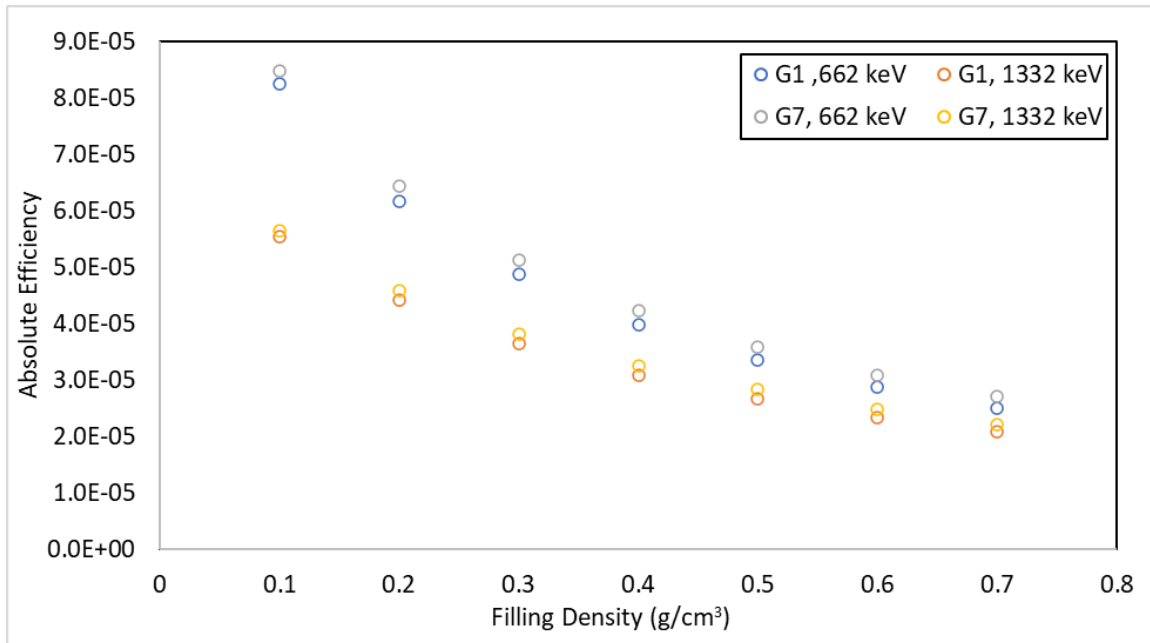


Figure 31: Absolute efficiency comparison between Group 1 and Group 7 materials at various filling densities. Both 662 keV photon and 1332 keV photon are tested.

5.3 Hotspot Simulation and Detector Array Design

All the previous studies assume that the waste activity is evenly distributed throughout the whole container volume. This assumption will be too generous for the incoming unsorted waste containers, as only a portion of the waste bags is heavily contaminated. To imitate the uneven distribution of the contamination, I designed a Hotspot model to study. The hotspot model consists of a 10x10x10 cm size cube that contains the radiation, while the rest of the space is filled with non-radioactive materials which just act as attenuators. There are 27 hotspot locations in total which cover the three different locations on each axis. The inner volume of the container has the dimension of 182.32(x)×101.83(y) ×118.82(z) cm, and the

occupied range in the model are $x=-91.16\sim 91.16$, $y=-59.41\sim 59.41$, $z=10.28\sim 129.1$. Three locations on each axis are chosen as hotspots, the 10 cm on the near and far ends, plus the 10 cm in the middle of the axis. By combining the 3 locations on each axis, we will end up with 27 different locations that are evenly distributed into the volume.

The location for hot spots is described in order of z, y, and x-axis (the front detector is facing the positive z direction). For example, hotspot #1 is described as “far, top, left”, which means the contamination is at the far end, top row, and left end of the container. For hotspot #18, a “mid, bottom, right” location means the contamination is at the middle line of the z-axis, the bottom of the container, and the right end of the detector. The 2D plot for the contamination locations for hotspots #1 and #18 is displayed in [Figure 32](#). The detailed location of each hotspot and a 3D depiction of the locations is provided in the [Appendix](#).

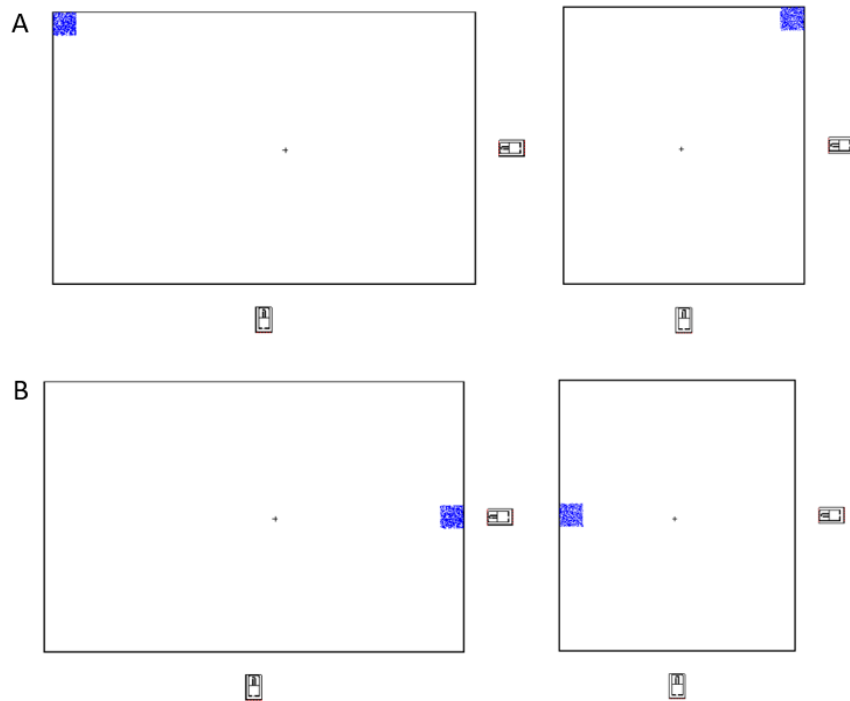


Figure 32: The 2D plot for hotspot location of #1 (A) and #18 (B) in Visual Editor software. The left graphs are on the x-z plane, and the right graphs are on the y-z plane. The detectors at the bottom are the front detector, which faces the positive z-axis.

To investigate the relation between the contamination location and the detector response, the simulation is run on each hotspot location to acquire data. A single detector at a stationary location can be used in this study, but when the measurement is taken in the radiation zone in reality, the high background will overshadow the weak detector response when the contamination is farther from the detector. Therefore, detectors need to be placed at different locations to simulate the response on the same hotspot location, and the detector responses are then compared.

Two detector arrays are built on the non-processible waste container model (shown in [Figure 33](#)). Considering the complexity of the system and the high cost of the radiation detector in real life, the detector array I chose to simulate consists of 3 HPGe detectors rather than the one mentioned in [Section 5.1](#). **Array 1** is made up of HPGe detectors placed at the center of the front, top, and right surfaces, while **Array 2** has three HPGe detectors placed diagonally at each surface. All the detectors are placed 10 cm from the container in this simulation. The density of the inner container volume is set to 0.2 g/cm³ to keep the model consistent.

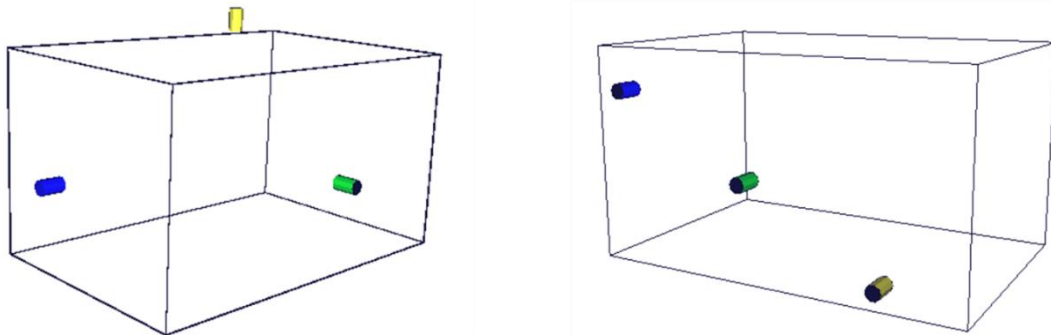


Figure 33: The 3D structure of multi-detector Array 1 (left) and Array 2 (right). The visual editor displays mirrored images in 3D display, and the blue detector (left) is coded to be at the opposite surface.

5.4 Detector Array Response Analysis

In MCNP, the F8 tally is run on each detector separately, and the simulated 662 keV full energy peaks are compared at each hotspot. For **Array 1**, the absolute efficiency result is plotted in [Figure 34](#) as it compares the detector responses against the distance from the center of the hotspot to the corresponding three detector surfaces.

10E10 particles are simulated in MCNP for every hotspot location so that the statistical uncertainty increases as the detection efficiency decreases. When the source-to-detector distance is longer than 150 cm, the uncertainty will be greater than 1%. However, the data at a longer distance is less contributive to us since the weak detector response will be easily obscured by the background noise during an on-site measurement.

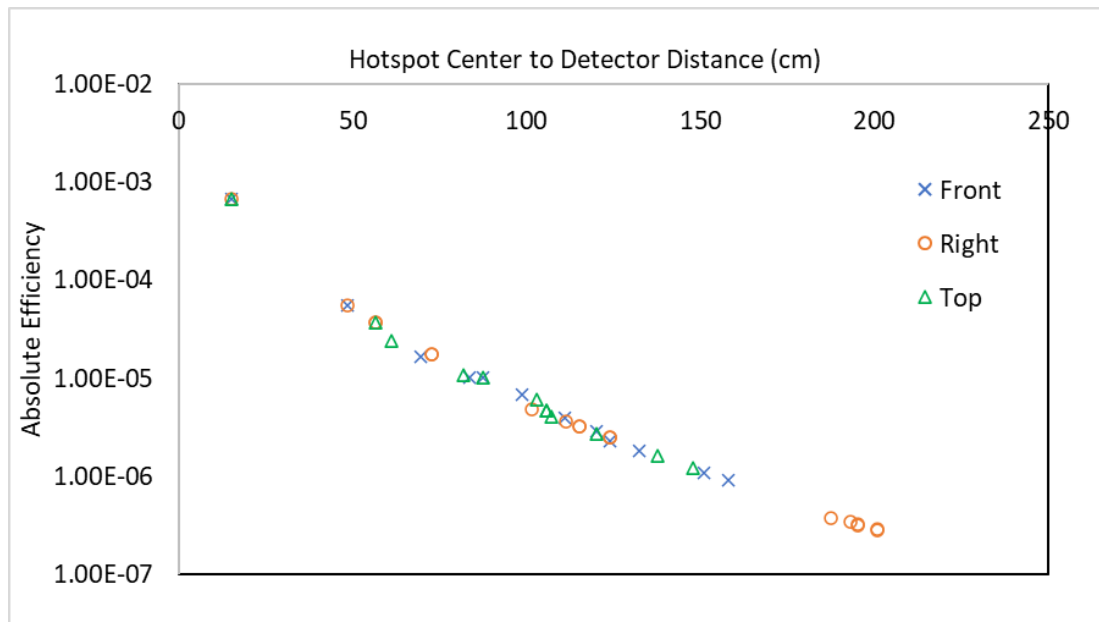


Figure 34: Detector efficiency as a function of hotspot center location for the three detectors. The y-axis is plotted in a log scale. The waste density is 0.2g/cm³.

Regardless of the location of the detector or hotspots, the detection efficiency is impacted by the source-to-detector distance in a similar way as all the data points can form a trendline. This trendline can be best fitted by two different functions, where $y \propto x^{-3.05}$ has an R² value of 0.9971 and $y \propto e^{-0.038x}$ has an R² value of 0.9528. This result is expected, as the photon detection will be affected by the

inversed-square law based on the distance of the source, as well as the attenuation during the traveling path which follows the Beer-Lambert Law $y \propto e^{-\mu x}$. For the sources that are closer to the detector, less attenuation will happen due to the shorter path, which will result in the trendline looking closer to a power function. As the source distance increases, the Beer-Lambert Law has more impact, which results in a curve similar to the exponential relation.

Another series of simulations were also performed on the same detector array and hotspot location, except the density of the filling material was increased to 0.5 g/cm^3 ([Figure 35](#)). The general trendlines still follow the observation with the 0.2 g/cm^3 model, but with the efficiency curve shifted down as more attenuation happens in denser material. Interestingly, there are a few outliers that do not follow the trend, which is indicated by an arrow. This can be caused by the 10 cm distance from the detector to the containers. As for the hotspot locations that have higher absolute efficiency than the trend, they are all located on the surface of the container.

Therefore, a part of the photons that reach the detector will have air as the major attenuator, which will result in much lower attenuation than the ones that need to travel through the container. As the density of the filling material increases, a greater difference between the outliers and the main trend will be observed. This might be improved by moving the detectors closer to the container to minimize the photon traveling path in the air. Another method is to move the hotspots further away from the surface so that the denser filling material will contribute more to total attenuation.

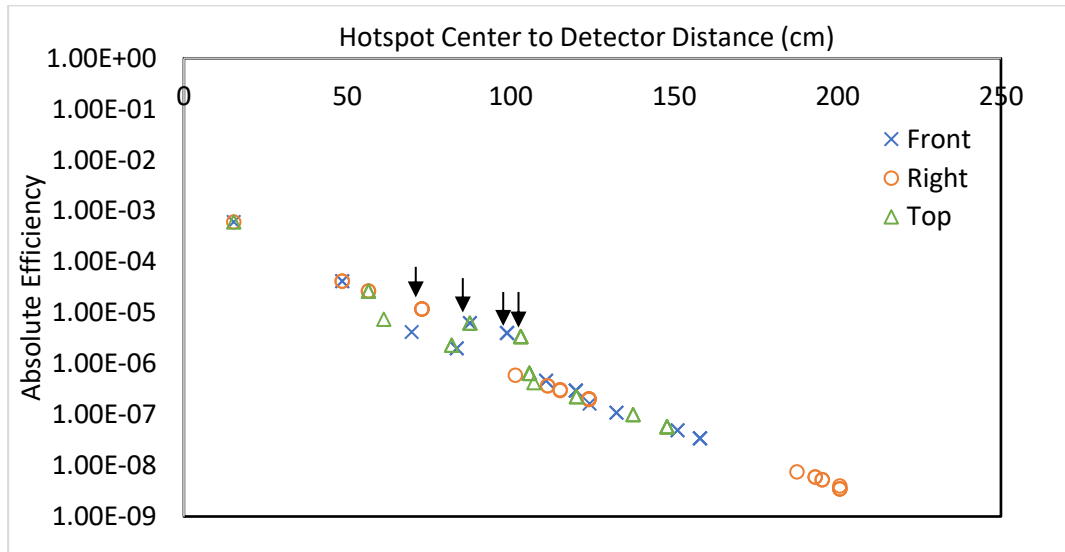


Figure 35: Detector efficiency as a function of hotspot center location for the three detectors. The y-axis is plotted in a log scale. The waste density is 0.5g/cm³. The outliers are indicated by arrows.

To provide better visualization of the data, the ratio between the absolute efficiency of each detector is taken relative to the front detector at every hotspot position. This ratio relation is shown in [Table 12](#), with the uncertainty on each value within 1%. Comparing the ratios at each location for the two densities, the higher density of the attenuator further magnifies the higher efficiency and reduces the lower efficiency. Using Position #18 as an example, at lower density, the right detector has the highest efficiency ratio of 19.07, while the top detector has the lowest efficiency ratio of 0.57. As density increases, the relative ratio for the right and top detector change to 141.99 and 0.34.

Since the detector location covers all three dimensions, the detector response when placed on the other three surfaces (back, left, bottom) can be derived based on

symmetry. For example, the detector response for hotspot #1 on the back surface will be the same as the front detector response for hotspot #21. This can save a significant amount of computation time when modifying this system.

Table 12: The absolute efficiency of each detector position on hotspots relative to the front detector

0.2 g/cm ³				0.5 g/cm ³			
Position #	Front/Front	Right/Front	Top/Front	Position #	Front/Front	Right/Front	Top/Front
1	1.00	0.31	6.49	1	1.00	0.10	99.73
2	1.00	1.34	19.92	2	1.00	1.87	244.91
3	1.00	19.27	6.49	3	1.00	344.43	99.73
4	1.00	0.30	4.24	4	1.00	0.11	13.33
5	1.00	1.42	4.65	5	1.00	1.81	14.06
6	1.00	33.46	4.24	6	1.00	544.70	13.33
7	1.00	0.31	1.32	7	1.00	0.10	1.68
8	1.00	1.34	1.49	8	1.00	1.87	2.07
9	1.00	19.27	1.32	9	1.00	344.43	1.68
10	1.00	0.12	3.50	10	1.00	0.02	21.26
11	1.00	0.36	66.27	11	1.00	0.18	304.67
12	1.00	19.07	3.50	12	1.00	141.99	21.26
13	1.00	0.10	1.19	13	1.00	0.02	1.41
14	1.00	0.30	1.47	14	1.00	0.14	1.79
15	1.00	170.68	1.19	15	1.00	1315.06	1.41
16	1.00	0.12	0.57	16	1.00	0.02	0.34
17	1.00	0.36	0.40	17	1.00	0.18	0.21
18	1.00	19.07	0.57	18	1.00	141.99	0.34
19	1.00	0.04	0.87	19	1.00	0.00	0.86
20	1.00	0.04	0.66	20	1.00	0.00	0.63
21	1.00	2.60	0.87	21	1.00	2.96	0.86
22	1.00	0.03	0.46	22	1.00	0.00	0.10
23	1.00	0.00	0.02	23	1.00	0.00	0.00
24	1.00	3.61	0.46	24	1.00	4.24	0.10
25	1.00	0.04	0.18	25	1.00	0.00	0.01
26	1.00	0.04	0.05	26	1.00	0.00	0.01
27	1.00	2.59	0.18	27	1.00	2.94	0.01

**The photon energy used for simulation is 662 keV*

For **Array 2** (3 diagonal detectors), the simulation is performed on the detector at 9 different positions (on 3 surfaces) in total. However, only 12 hotspot locations are simulated due to time pressure. The efficiency at each detector is acquired similarly to **Array 1**, but the detector result on each surface is processed separately. At each surface, the simulated efficiency for the center detector is used as the reference point, where the ratio of the other two detectors is taken relative to the center value. This method is more organized, as the approximate region of the hotspot can be predicted by comparing the results of the 3 detectors at the same surface. Using the hotspot #4 result as an example, if the front measurement result shows a similar pattern to 2.45:1:0.14, we will know that the position of the hotspot is likely to be at the left half of the container. Then using the ratios from the top detector and right detector array, we can approximate the location in a 3D coordinate. The simulation result is presented in Table 13.

Table 13: The absolute efficiency relative to the center detector (#2) at each surface

Hotspot Position	Front Surface			Top Surface			Right Surface		
	F1	F2	F3	T1	T2	T3	R1	R2	R3
4	2.45	1.00	0.14	0.07	1.00	4.63	0.54	1.00	1.04
5	0.45	1.00	0.44	0.09	1.00	0.74	0.26	1.00	1.48
7	1.38	1.00	0.18	0.10	1.00	32.45	0.64	1.00	1.00
8	0.29	1.00	0.78	0.09	1.00	0.67	0.43	1.00	0.72
10	10.58	1.00	0.05	0.11	1.00	5.96	0.85	1.00	0.42
11	0.58	1.00	0.13	0.02	1.00	0.02	1.08	1.00	0.30
13	4.75	1.00	0.07	0.07	1.00	4.63	0.63	1.00	0.68
14	0.21	1.00	0.21	0.15	1.00	0.15	0.53	1.00	0.53
23	0.02	1.00	0.02	0.74	1.00	0.09	1.41	1.00	0.26
24	0.11	1.00	7.88	15.41	1.00	0.05	2.65	1.00	0.14
26	0.09	1.00	0.44	0.82	1.00	0.18	0.72	1.00	0.45
27	0.11	1.00	30.26	5.96	1.00	0.07	0.66	1.00	0.38

*The assigned number represents the detector position on the surface, where 1 is the top-left, 2 is the center, and 3 is the bottom-right.

*The material filling density is set at 0.5 g/cm³, and the photon energy is 662 keV.

5.5 Blind Test for Array 1 Model

A simple blind test is conducted for the **Array 1** result to verify the accuracy. Four 10×10×10 cm hotspots are created where the locations do not belong to any of the 27 hotspots in the chart. The information on the new hotspots and the simulated result is included in [Table 14](#). The filling density used in this test is 0.5 g/cm³, as the higher density makes the test result more sensitive to distance.

Table 14: The Hotspot Locations used for the blind test and the simulation result

Blind Test Hotspot #	Location Description	Hotspot Center Coordinates	Front/Front	Right/Front	Top/Front
1	between #4 and #5	(-30, 0, 124.1)	1.00	0.43	11.79
2	between #14 and #15	(30, 0, 70)	1.00	1.27	1.71
3	between #10 and #11	(-35, 40, 50)	1.00	0.01	9.19

4	between #16 and #25	(-60, -32, 50)	1.00	0.01	0.17
---	------------------------	----------------	------	------	------

By comparing the blind test ratio result to the hotspot simulation data from [Table 12](#), a general estimation of the hotspot position is made. Through the comparison, the locations for blind tests #1, #3, and #4 can be predicted to be nearby hotspots #4, #10, and #16, respectively. However, the prediction for blind test #2 failed as the efficiency ratio is completely different from the result of hotspot #16 or #25.

Furthermore, the correct predictions do not provide a precise location. Using test #1 as an example, I cannot predict the location in between hotspot #4 and #5 as the Right/Front ratio change too rapidly from 0.11 to 1.81.

This phenomenon can be caused by two reasons from the original hotspot model design: First, the hotspots that locate at the surfaces of the container cause a rapid increase in efficiency compared to the hotspots that are deeper into the container. The attenuation of air is negligible compared to the attenuation of the filling material. Second, the number of hotspots used in this test is insufficient, which causes the distance between the hotspots to be too large. This will contribute to big differences in the efficiency ratio due to the rapid decrease in absolute efficiency, which is discussed in [Figure 35](#) result. Therefore, the large difference between the hotspot and the adjacent hotspots will make the decision difficult.

5.6 LEP Waste Container Measurement and Comparison with Hotspot Model

An on-site measurement was performed on the container filled with sorted waste at LEP's low background surveying area. It is located at the northeast corner of the building, beside the container storing area. The area is shielded by cement walls to minimize the high background level from waste storage. The LaBr₃ detector with the pre-amplifier was used, and the corresponding MCNP model was developed. The waste container information is listed in [Table 15](#).

Table 15: Information for the measured container

Bin Type	Dimension	Shielding Thickness	Empty Container Weight	Total Weight	Waste Type	Filling Density
Green bin (high-capacity non-processible container)	182.88(L) × 119.38(W) × 74.45(H) cm	0.28 cm	325 kg	668.1 kg	Compatible (glass bottles)	0.143 g/cm ³

Based on the simulation result obtained from **Section 5.3 and 5.4**, the detector and hotspot locations are modified to reduce the “outliers” situation we encountered previously. The detectors are placed directly onto the container rather than having a 10 cm gap. This will be much easier to achieve in practice since no other equipment would need to be used to stabilize the detector. The hotspot locations are slightly changed as well. I divided the container volume into 27 parts equally and placed the 10x10x10 cm hotspot at the center of each part. In this case, the hotspots are not

located directly along the container wall, which will now introduce more attenuation for the photons before reaching the air and reduce the value of the outliers. The 2D plots for hotspots #1 and #18 are shown in [Figure 36](#) below.

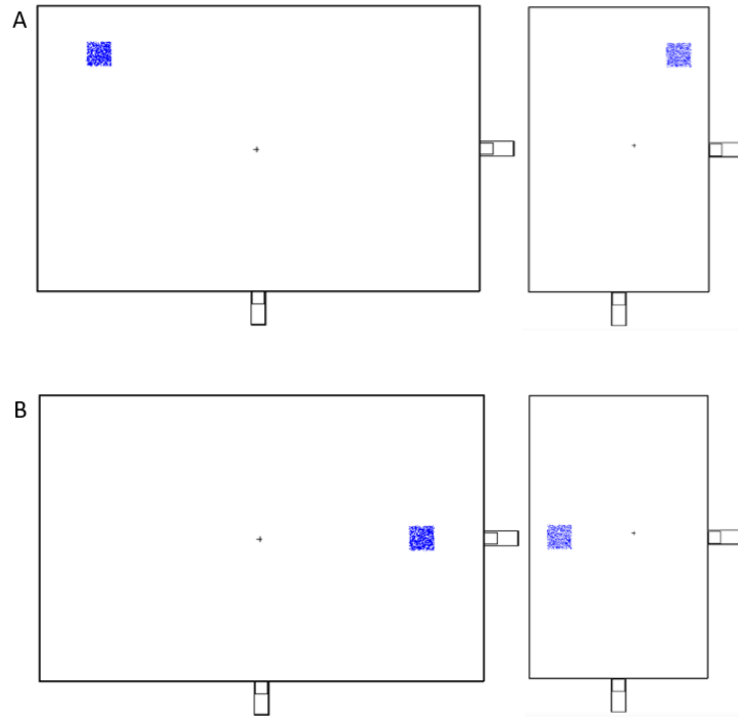


Figure 36: The 2D plot for the updated hotspot location of #1 (A) and #18 (B) in Visual Editor software. The left graphs are on the x-z plane, and the right graphs are on the y-z plane. The detectors at the bottom are the front detector, which faces the positive z-axis.

The detector's responses at the centers of the front, right, and top surfaces are simulated and compared, similar to **Section 5.4**. Since we have access to 5 surfaces of the container during measurements, the absolute efficiency of the detector at the left and back surfaces is also included using the symmetry of the hotspots. The

efficiency ratio at different detector positions is taken relative to the top detector efficiency. Both the 662 keV and 1173 keV photons are simulated for the possible existence of Cs-137 and Co-60. The ratio values are organized in Table 16.

Table 16: The absolute efficiency of each detector position on the new hotspots model for 662 keV and 1173 keV photons.

Hotspot #	662 keV					1173 keV				
	Front	Right	Top	Back	Left	Front	Right	Top	Back	Left
1	0.38	0.13	1.00	1.51	4.09	0.39	0.15	1.00	1.41	3.47
2	0.09	0.10	1.00	2.08	0.10	0.11	0.11	1.00	1.95	0.11
3	0.38	4.07	1.00	1.51	0.13	0.38	3.46	1.00	1.41	0.15
4	0.37	0.12	1.00	1.67	5.10	0.40	0.15	1.00	1.65	4.54
5	0.28	0.29	1.00	14.49	0.29	0.31	0.32	1.00	12.90	0.32
6	0.45	6.19	1.00	2.03	0.15	0.48	5.49	1.00	1.98	0.18
7	0.51	0.17	1.00	2.04	5.49	0.54	0.21	1.00	2.00	4.88
8	0.37	0.37	1.00	8.14	0.37	0.40	0.40	1.00	7.30	0.40
9	0.51	5.46	1.00	2.04	0.17	0.55	4.88	1.00	1.99	0.21
10	0.55	0.08	1.00	0.55	6.66	0.54	0.10	1.00	0.54	5.59
11	0.03	0.01	1.00	0.03	0.01	0.03	0.01	1.00	0.03	0.01
12	0.55	6.65	1.00	0.55	0.08	0.54	5.60	1.00	0.54	0.10
13	0.64	0.09	1.00	0.65	13.72	0.66	0.11	1.00	0.66	11.89
14	0.31	0.09	1.00	0.31	0.09	0.33	0.11	1.00	0.33	0.11
15	0.64	13.64	1.00	0.64	0.09	0.66	11.87	1.00	0.66	0.11
16	0.94	0.14	1.00	0.94	11.35	0.94	0.18	1.00	0.94	9.75
17	0.92	0.31	1.00	0.92	0.31	0.92	0.33	1.00	0.92	0.33
18	0.94	11.35	1.00	0.94	0.14	0.94	9.74	1.00	0.94	0.18
19	1.52	0.13	1.00	0.38	4.08	1.41	0.15	1.00	0.38	3.47
20	2.08	0.10	1.00	0.09	0.10	1.95	0.11	1.00	0.11	0.11
21	1.51	4.07	1.00	0.38	0.13	1.41	3.45	1.00	0.39	0.14
22	1.67	0.12	1.00	0.37	5.12	1.65	0.15	1.00	0.40	4.58
23	9.19	0.18	1.00	0.17	0.18	8.42	0.21	1.00	0.20	0.21
24	1.67	5.10	1.00	0.37	0.12	1.65	4.54	1.00	0.40	0.15
25	2.04	0.17	1.00	0.52	5.49	2.00	0.21	1.00	0.55	4.90
26	8.14	0.37	1.00	0.37	0.37	7.29	0.40	1.00	0.40	0.40
27	2.04	5.48	1.00	0.51	0.17	2.00	4.89	1.00	0.55	0.21

The measurement of the waste container consists of two parts. First, the contact dose rates were collected using the BOT 2000 gamma surveyor. Each surface of the container was divided into 6 sextants, and the highest dose rate for each was recorded. Based on the information provided by the sorting team, 2 bags of waste contain activities over 15 MBq. While the rest of 33 bags contain activities lower than 3 MBq. However, the locations of the bags are unknown. To describe the locations on the container more conveniently, the surface with the LEP sticker is defined as the “front” surface, with the rest named accordingly. With dose rate surveying, one hotspot was located with a contact dose rate of 1.2 mrem/h. The location of the main hotspot and the side naming system are described in [Figure 37](#). Other than this hotspot, there are several hotspots on the left and back surfaces with the highest dose rate of 0.86 mrem/h. The detailed dose rate survey result taken by the radiation surveyor can be found in the [Appendix](#).



Figure 37: The location of the hotspot is indicated by the red box.

The gamma spectrum collection is then performed on the center of the 5 surfaces, with the detector surface directly on the bin. The sufficient collection time is taken to ensure the photon peak area of interest is greater than 10,000 counts to keep the statistical uncertainty low. [Figure 38](#) shows the spectrum collection process for the top center location. The collected spectrum is then analyzed to obtain the net count by subtracting the linear background counts using the CAEN Compass software. The spectrum for the back center location is shown in [Figure 39](#) as an example. The count rate at each location is then calculated, and the ratio between the values is calculated relative to the top center location result. The count rate ratio for the 662 keV, 1173 keV, and 1332 keV peaks are listed in [Table 17](#) with uncertainties less than 1%. This result will be used to compare to the [Table 16](#) result to locate the hotspot in the container.

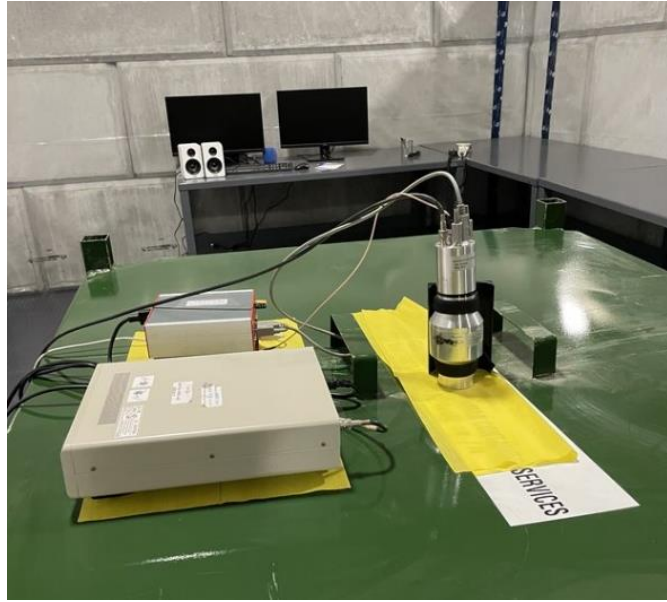


Figure 38: Gamma spectrum acquisition process at the top center position

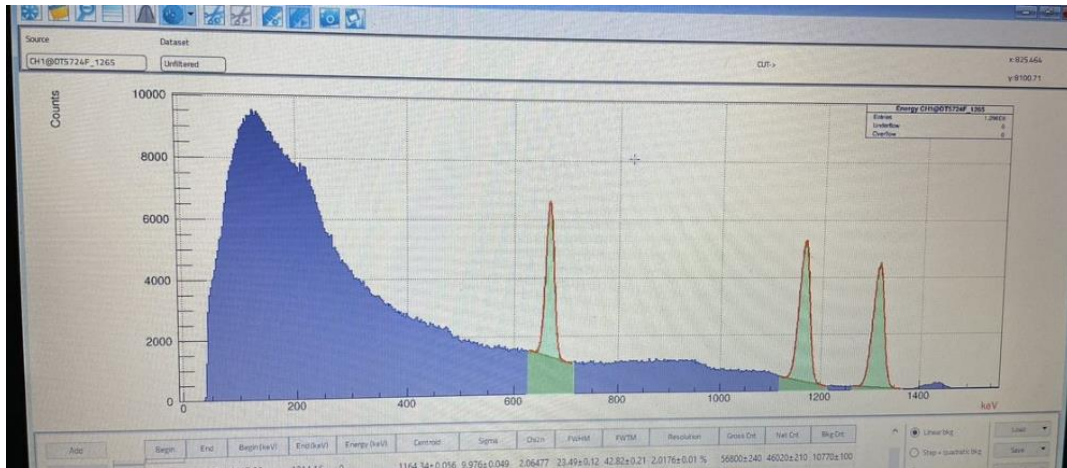


Figure 39: The 5-minute gamma spectrometry collected at the center of the back surface. The three highlighted peaks are the Cs-137 and Co-60 photons.

Table 17: The ratio of the count rate at each location relative to the top location

Energy (keV)	Front	Right	Top	Left	Back
662	0.97	3.68	1	1.62	1.23

1173	0.47	0.13	1	0.05	0.22
1332	0.48	0.13	1	0.05	0.22

Based on the measurement result for Cs-137, both the left and right locations have higher count rates than the top location, while the other two count rates are also similar to the top location. Using the ratio values from Table 16, the hotspots with the most similar ratios to the ratio chart are #12 and #15. However, the values for the back and left detectors are not accurate. Referring to the dose rate surveying result, no increasing dose rate was found at the right surface, while the high dose rate from the top surface is not reflected in the Cs-137 spectrums. As a result, two hypotheses can be made for the Cs-137 distribution. The first one is that the Cs-137 contamination has multiple small hotspots or a large hotspot throughout the volume, which results in a high response from multiple surfaces. The second one is that the hotspot is located at the bottom of the container, such as below hotspot #17. Such a case, the contamination can still contribute sufficient signal to the detector at the 4 sides while taking the path with the highest attenuation to reach the top detector.

On the other hand, the distribution for the Co-60 is more straightforward to predict. Based on the ratio result, the top detector has the highest response compared to the others. From the ratio result for 1173 keV photons, hotspots #11 and #14 have the most similar pattern. Furthermore, the hotspot location in the dose rate survey report can support our gamma spectrometry prediction. As the highest dose rate is

found close to the center of the top surface, it indicates the contamination does not locate too far below the top surface. This matches our prediction of hotspot #11 and #14.

Overall, this multi-detector array model for locating hotspots in volume wastes still needs further development. The current model has reasonable accuracy when surveying samples that have a single hotspot and relative uniform density distribution. A more extensive study needs to be done to include detector responses from different hotspot sizes and distribution patterns. In terms of the applicability in waste sorting procedures, this model is not good enough to be used for incoming unsorted CANDU waste characterization due to the complexity of the waste materials. However, there are still a few potential applications for this algorithm. One of the possible applications is on the free-releasable waste prior to discharge, where the clean low self-attenuated wastes need to be shredded for packaging. The clean wastes are surveyed through the Large Article Monitor (LAM) to ensure the activity concentration is below the free-release standard. Since the shredding process turns the waste into uniform density, my detector array can perform well in looking for any potential hotspots before releasing, which ensures the LAM result. Another possible application is for qualitative and quantitative analysis similar to the ISOCS/LabSOCS software. For the different densities of the container, correction factors can be developed to turn the measured activity of radioisotopes into real activities. As the MCNP algorithm is more versatile in waste geometry and

distribution design, it has the potential to outperform the current commercial software.

Chapter 6: Conclusion and Future Works

6.1 Conclusion

To acquire real-time source term information from the CANDU low-level waste containers, an MCNP-based model is developed to simulate the gamma spectrum of the N-type coaxial HPGe detector and the 2" by 2" LaBr₃ detector. The MCNP model for the HPGe detector has been validated with the point, disk, and volumetric sources. The F8 tally result shows high accuracy of the peak absolute efficiency for photon energy greater than 500 keV. Compared to the Mirion ISOCS/LabSOCS software, this model can provide better activity estimation on volume sources with complex geometry and uneven waste distribution.

Additionally, the MCNP model of two multi-detector arrays was developed to simulate the detector responses at different locations of the 2.2 m³ waste containers. A hotspot model was used to collect and compare the detector responses. The results are summarized in a table that shows the energy peak efficiency on each detector for the hotspot location. Compared to the on-site measurement result, this model can locate the hotspot within the volume of 61×40×34 cm. However, the current detector array model has not demonstrated the ability to measure containers that have inconsistent or high-density objects, limiting its use to incinerable bins, where the materials have relatively low density and are evenly distributed.

6.2 Future Work

The MCNP model for the HPGe detector has good accuracy for the medium to high energy range, while the peak efficiencies for photon energy less than 500 keV are significantly different than the experimental result. The MCNP model for the detector and the calibrated sources needs to be further investigated, as low-energy photons are sensitive to additional attenuation materials. This can be done through using low-energy gamma sources with a simple decay scheme to minimize the low-energy background counts.

The hotspots model needs to be further studied since the 27 hotspots do not provide enough details for precise analysis. A more extensive database can be built by simulating responses for hotspots with different sizes and locations. Machine Learning can be a great tool to assist this topic as the relationship between simulated responses and experimental result can be difficult to associate.

The multi-detector array can also be further developed. New detector variants can be added to create an array made up of different types of radiation detectors. As for the current model, it was only tested to be used to measure samples with relatively consistent density. The data analysis can be limited if there is a sudden increase in density where the contamination is (e.g., a contaminated piece of metal in the container). Therefore, the volume source model can be further studied by modifying the material and the density distribution of the volume source.

Bibliography

- [1] C. E. R. Government of Canada, 'CER – Provincial and Territorial Energy Profiles – Ontario', Jul. 28, 2022. <https://www.cer-rec.gc.ca/en/data-analysis/energy-markets/provincial-territorial-energy-profiles/provincial-territorial-energy-profiles-ontario.html> (accessed Mar. 05, 2023).
- [2] C. N. Safety Commission, 'Low- and intermediate-level radioactive waste', Feb. 03, 2014. <http://nuclearsafety.gc.ca/eng/waste/low-and-intermediate-waste/index.cfm#low-level> (accessed Mar. 05, 2023).
- [3] 'Radioactive Wastes - Myths and Realities : World Nuclear Association - World Nuclear Association'. <https://world-nuclear.org/information-library/nuclear-fuel-cycle/nuclear-wastes/radioactive-wastes-myths-and-realities.aspx> (accessed Mar. 05, 2023).
- [4] 'Laurentis and McMaster's Clean Energy Sorting and Recycling Initiative is making strides » Laurentis Energy Partners', *Laurentis Energy Partners*. Accessed: Mar. 06, 2023. [Online]. Available: <https://laurentisenergy.com/story/laurentis-and-mcmasters-clean-energy-sorting-and-recycling-initiative-is-making-strides/>
- [5] F. Bronson, V. Atrashkevich, G. Geurkov, and B. Young, 'Probabilistic uncertainty estimator for gamma-spectroscopy measurements', *J Radioanal Nucl Chem*, vol. 276, no. 3, pp. 589–594, Jun. 2008, doi: 10.1007/s10967-008-0604-z.
- [6] L. Bourva *et al.*, 'An Advanced ISOCS In Situ Gamma Spectrometry Services Tool to Reduce Uncertainties in Waste Characterization Projects - 16311', presented at the WM2016: 42 Annual Waste Management Symposium, United States, 2016.
- [7] 'S573 ISOCS™ Calibration Software'. <https://www.mirion.com/products/s573-isocs-calibration-software> (accessed Mar. 13, 2023).
- [8] *Strategy and Methodology for Radioactive Waste Characterization*. in TECDOC Series, no. 1537. Vienna: INTERNATIONAL ATOMIC ENERGY AGENCY, 2007. [Online]. Available: <https://www.iaea.org/publications/7655/strategy-and-methodology-for-radioactive-waste-characterization>
- [9] N. Estre, D. Eck, J.-L. Pettier, E. Payan, C. Roure, and E. Simon, 'High-energy X-ray imaging applied to non destructive characterization of large nuclear waste drums', in *2013 3rd International Conference on Advancements in Nuclear Instrumentation, Measurement Methods and their Applications (ANIMMA)*, 2013, pp. 1–6. doi: 10.1109/ANIMMA.2013.6727987.
- [10] B. Pérot *et al.*, 'The characterization of radioactive waste: a critical review of techniques implemented or under development at CEA, France', *EPJ N - Nuclear Sciences & Technologies*, vol. 4, p. 3, 2018, doi: 10.1051/epjn/2017033.
- [11] M. Fang, Y. Altmann, D. Della Latta, M. Salvatori, and A. Di Fulvio, 'Quantitative imaging and automated fuel pin identification for passive gamma emission

- tomography', *Sci Rep*, vol. 11, no. 1, Art. no. 1, Jan. 2021, doi: 10.1038/s41598-021-82031-8.
- [12] T. T. Thanh *et al.*, 'A prototype of radioactive waste drum monitor by non-destructive assays using gamma spectrometry', *Applied Radiation and Isotopes*, vol. 109, pp. 544–546, Mar. 2016, doi: 10.1016/j.apradiso.2015.11.037.
- [13] G. F. Knoll, *Radiation detection and measurement*, 4th ed. Hoboken, N.J.: John Wiley, 2010.
- [14] 'Gamma-X (GMX) N-type High Purity Germanium HPGe Coaxial Radiation Detectors | AMETEK ORTEC'. <https://www.ortec-online.com/products/radiation-detectors/germanium-hpge-radiation-detectors/hpge-radiation-detector-types-how-choose/gmx-n-type-coaxial-hpge-radiation-detectors> (accessed Mar. 27, 2023).
- [15] D. T. Vo, P. A. Russo, and T. E. Sampson, 'Comparisons between digital gamma-ray spectrometer (DSpec) and standard nuclear instrumentation methods (NIM) systems', Los Alamos National Lab. (LANL), Los Alamos, NM (United States), LA-13393-MS, Mar. 1998. doi: 10.2172/654106.
- [16] T. Ren, 'Solving the Extremely High Dead Time During Ultra-High-rate Gamma-ray Spectrometry Using a LaBr₃(Ce) Detector', McMaster University, 2022.
- [17] A. LARANJEIRO, 'The Characterization and Optimization of a LaBr₃(Ce) Spectroscopy System for High-rate Spectrometry at CANDU Reactors', McMaster University, 2018.
- [18] 'TECHNICAL BASIS FOR ACTIVITY CALCULATION OF ROUTINE RADIOACTIVE LOW LEVEL WASTE SHIPMENTS'. Ontario Power Generation.
- [19] N. Metropolis, 'THE BEGINNING of the MONTE CARLO METHOD', Accessed: Mar. 15, 2023. [Online]. Available: <https://www.semanticscholar.org/paper/THE-BEGINNING-of-the-MONTE-CARLO-METHOD-Metropolis/9630fe755a64231a69519b771fb744d540d626e9>
- [20] C. J. Werner, 'MCNP User's Manual Code Version 6.2.', Los Alamos National Lab. (LANL), Los Alamos, NM (United States), LA-UR-17-29981, Oct. 2017. Accessed: Mar. 28, 2023. [Online]. Available: https://mcnp.lanl.gov/pdf_files/TechReport_2017_LANL_LA-UR-17-29981_WernerArmstrongEtAl.pdf
- [21] S. H. Byun, 'EGS5 Result_ORTEC_HPGe Drawing_SN40-P31455A_25cm_DeadLayer 1.5 mm thick', Jun. 21, 2022.
- [22] C. C. Conti, I. C. P. Salinas, and H. Zylberberg, 'A detailed procedure to simulate an HPGe detector with MCNP5', *Progress in Nuclear Energy*, vol. 66, pp. 35–40, Jul. 2013, doi: 10.1016/j.pnucene.2013.03.003.
- [23] 'Overview of Semiconductor Photon Detectors ORTEC',
- [24] R. S. Detwiler, R. J. McConn, T. F. Grimes, S. A. Upton, and E. J. Engel, 'Compendium of Material Composition Data for Radiation Transport Modeling', Apr. 2021, doi: 10.2172/1782721.
- [25] R. Garnett, W. V. Prestwich, J. Atanackovic, M. Wong, and S. H. Byun, 'Characterization of a LaBr₃(Ce) detector for gamma-ray spectrometry for

- CANDU power reactors', *Radiation Measurements*, vol. 106, pp. 628–631, Nov. 2017, doi: 10.1016/j.radmeas.2017.03.042.
- [26] L. Li, Q. Alexander, and B. Van Der Ende, 'A METHOD FOR COINCIDENCE SUMMING COMPENSATION OF SIMULATION RESULTS USING MCNP ON Co60 VOLUME SOURCE', *CNL Nuclear Review*, pp. 1–5, Jun. 2016, doi: 10.12943/CNR.2015.00053.
- [27] O. Sima and D. Arnold, 'Accurate computation of coincidence summing corrections in low level gamma-ray spectrometry', *Applied Radiation and Isotopes*, vol. 53, no. 1, pp. 51–56, Jul. 2000, doi: 10.1016/S0969-8043(00)00113-5.
- [28] M. Pritchard, *NCS Approach for Decommissioning Low and Intermediate Level Waste Soils and Process Piping Using the InSpector 1000 with LaBr3*. 2013.

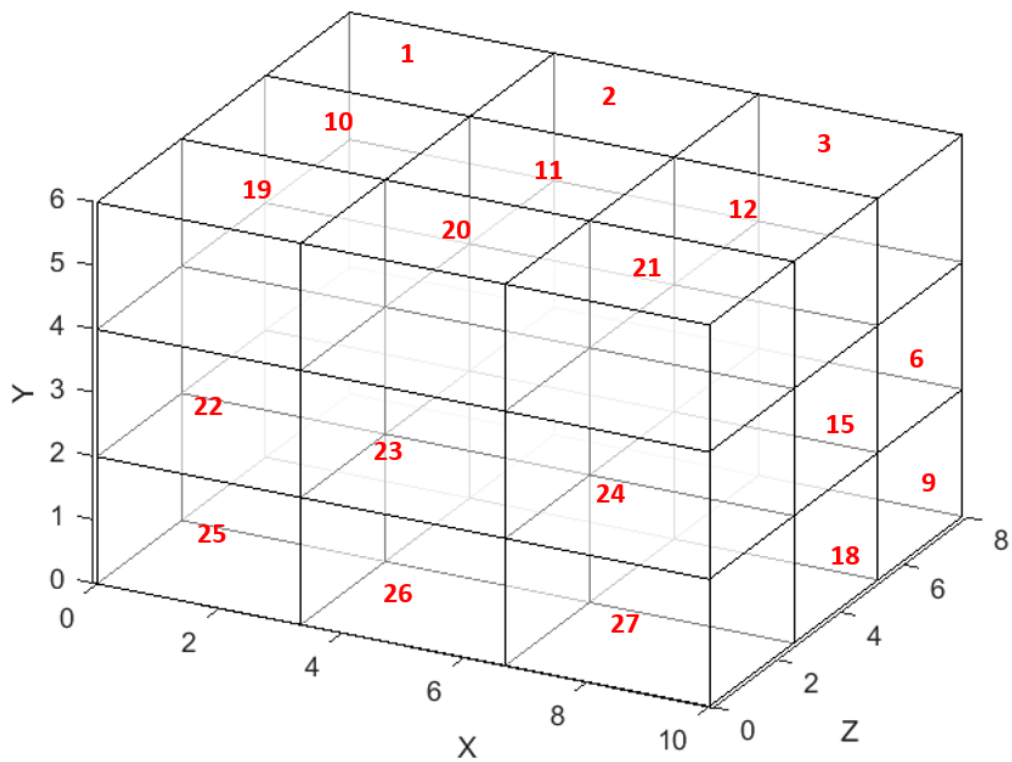
Appendix

1. Locations for the 27 hotspots built in the original hotspot model.

Assigned number	Position description (relative to front detector position)	center x	center y	center z
1	far top left	-86.16	45.915	124.1
2	far top mid	0	45.915	124.1
3	far top right	86.16	45.915	124.1
4	far mid left	-86.16	0	124.1
5	far mid mid (far center)	0	0	124.1
6	far mid right	86.16	0	124.1
7	far bot left	-86.16	-45.915	124.1
8	far bot mid	0	-45.915	124.1
9	far bot right	-86.16	-45.915	124.1
10	mid top left	-86.16	45.915	69.69
11	mid top mid	0	45.915	69.69
12	mid top right	-86.16	45.915	69.69
13	mid mid left	-86.16	0	69.69
14	mid mid mid (mid center)	0	0	69.69
15	mid mid right	-86.16	0	69.69
16	mid bot left	-86.16	-45.915	69.69
17	mid bot mid	0	-45.915	69.69
18	mid bot right	86.16	-45.915	69.69
19	near top left	-86.16	45.915	15.28
20	near top mid	0	45.915	15.28
21	near top right	86.16	45.915	15.28
22	near mid left	-86.16	0	15.28
23	near mid mid (near center)	0	0	15.28
24	near mid right	86.16	0	15.28
25	near bot left	-86.16	-45.915	15.28
26	near bot mid	0	-45.915	15.28
27	near bot right	86.16	-45.915	15.28

2. The front view for the hotspot locations in 3D coordinates. The hotspots are located inside the sub-volumes with the according numbers. For the original hotspot model used in the HPGe detector, the hotspots that are not in the center

(excluding 11, 14, 17) are located along the surface of the container. In the updated model used for the LaBr3 detector and field survey, the hotspots are located at the center of each sub-volume. The “Front Detector” is in front of Volume #23. The “Right Detector” is in front of Volume #15. The “Top Detector” is in front of Volume #11.



3. Dose rate survey result for the green compactable waste container at LEP. The hotspot locations are labeled in orange dots. The dose rate reported has the unit of mrem/h. The highest dose rate of the block is reported in the chart.

Top

0.75	1.23	1.27
0.69	1.40	1.13

Front

0.27	0.27	0.21
0.28	0.2	0.2

Back

0.36	0.51	0.38
0.39	0.42	0.32

Left

0.31		0.54
	0.65	
	0.86	0.7
0.46		

Right

0.37	0.31	0.31
	0.31	0.31
0.34	0.31	0.31